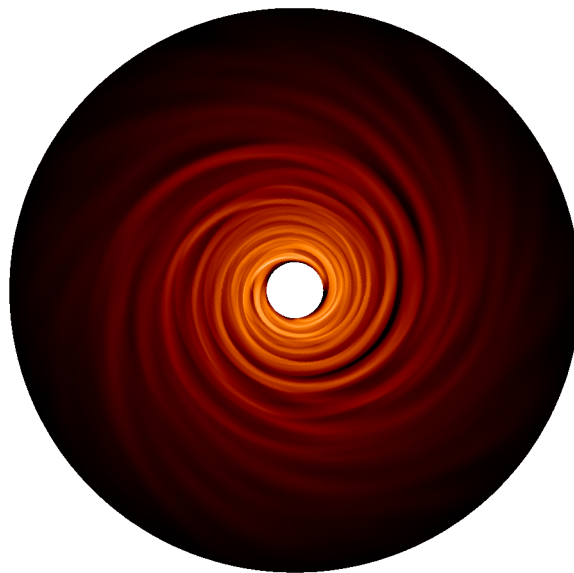


Self-gravitating Accretion Disks

Diplomarbeit von Tobias Müller



vorgelegt im Februar 2010

Institut für Astronomie und Astrophysik
Eberhard-Karls-Universität Tübingen
Abteilung Computational Physics

Erklärung gemäß § 18 (7) der Diplomprüfungsordnung

Hiermit erkläre ich, dass ich diese Arbeit selbständig verfasst und keine anderen als die angegebenen Quellen und Hilfsmittel benutzt habe.

Tübingen, 15. Februar 2010

Tobias Müller

Zusammenfassung

Die Entdeckung des ersten exosolaren Planeten (Mayor and Queloz, 1995) hat der Frage nach der Planetenentstehung neuen Auftrieb gegeben. Nachdem inzwischen viele weitere Planeten entdeckt wurden (siehe Abbildung 1.1), stellt sich insbesondere für sehr massereiche Planeten mit sehr großen Halbachse die Frage, wie diese entstanden sind, da diese mit der verbreiteteren Core-Accretion Theory nicht zu erklären sind. Eine Alternative stellt die Entstehung durch Gravitationsinstabilitäten dar, welche im Rahmen dieser Arbeit untersucht werden soll. Da bei dieser insbesondere die Kühlung der protoplanetaren Scheibe eine wichtige Rolle spielt, wird die Scheibe mit Berücksichtigung der Temperaturentwicklung simuliert.

Dazu werden selbst-gravitierende Akkretionsscheiben mit Hilfe des zweidimensionalen FARGO Codes simuliert, welcher dazu mit Routinen für die Eigengravitation erweitert wurde (Baruteau, 2008). Außerdem wurde zusätzlich eine Energiegleichung mit viskoser Heizung sowie lokaler Kühlung durch Wärmeabstrahlung implementiert. Dabei wurde für die viskose Heizung das α -Modell nach Shakura and Sunyaev (1973) für die Viskosität zu Grunde gelegt.

Zum Testen des Eigengravitation-Codes wurden im ersten Schritt isotherme Akkretionsscheiben, d. h. noch ohne Berücksichtigung der Energiegleichung, simuliert. Die Masse der Scheiben wurde dabei so gewählt, dass die Scheiben laut Toomre-Kriterium fragmentieren sollten, was in den Simulationen auch bestätigt werden konnte. Rechnungen mit leichteren Scheiben, welche das Toomre-Kriterium nicht erfüllen, fragmentierten nicht.

Im weiteren Teil wurde der Einfluss des Parameters α der Viskosität auf die Fragmentation der Scheibe mit Berücksichtigung der Heizung und Kühlung der Scheibe untersucht. Dabei stellten wir bei keinerlei Werten von α Fragmentation fest.

Im letzten Teil wurden noch Scheibenmodelle in Anlehnung eines Modells von Rice *et al.* (2005) simuliert. Während Rice *et al.* eine vereinfachte β -Kühlung und einen SPH (Smoothed Particle Hydrodynamics) verwendeten, rechneten wir die Modelle mit dem FARGO-Grid-Code und lokaler Kühlung durch Wärmeabstrahlung. Die Fragmentation der Scheibe des Modells von Rice *et al.* konnten wir mit der realistischeren Kühlung nicht bestätigen.

What happens if a big asteroid hits Earth? Judging from realistic simulations involving a sledge hammer and a common laboratory frog, we can assume it will be pretty bad.

David Barry

Contents

1	Introduction	9
1.1	Planetary formation	9
1.2	Outline	12
1.3	Notations	13
2	Theoretical foundations	15
2.1	Accretion disks	15
2.2	Hydrodynamics	16
2.2.1	Basic equations	16
2.2.2	Viscosity	16
2.2.3	Heat transport	17
2.3	Self-gravity	18
2.4	Thermodynamics	20
2.4.1	Estimation of cooling	21
3	Numerical methods	25
3.1	Introduction - FARGO	25
3.1.1	2D quantities	25
3.1.2	Code units	25
3.2	Finite differences	26
3.3	Staggered grid	27
3.4	The FARGO Algorithm	29
3.5	Boundary conditions	30
3.5.1	Open boundary	31
3.5.2	Reflecting boundary	31
3.5.3	Damping	32
3.6	Self gravity	32
3.7	Energy equation	35
3.8	Local radiative cooling	35
3.9	Tests	38
4	Results	41
4.1	Isothermal disk	41
4.2	Disks with cooling	49
4.2.1	Comparison with SPH models	53
5	Summary	59
	Acknowledgements	61
	References	63

1 Introduction

The discovery of the first exosolar planet (Mayor and Queloz, 1995) has triggered a gold rush for the discovery of exosolar planets. Over 400 exosolar planets have been discovered right now. Surprisingly the distribution of mass and semi-major axis of the exosolar planets (see figure 1.1) is different to the distribution in the solar system. This reignited the discussion of the formation of these planets especially between the standard model of core accretion and the disk instability theory.

1.1 Planetary formation

The first theories of planetary formation emerged in the 18th century. In 1755 Immanuel Kant (1724–1804) proposed his theory in his book “Allgemeine Naturgeschichte und Theorie des Himmels” and Pierre-Simon Laplace (1749–1827) independently proposed his theory in the last book of his series “Exposition du systeme du monde” in 1796.

According to Kant and Laplace, planets form out of a cold disk of gas and dust rotating around the star. Both theories were combined by Arthur Schopenhauer (1788–1860) to the Kant-Laplace theory. Nowadays, their basic ideas are the fundament of the modern standard model for stellar formation.

In modern standard model there is a massive, rotating molecular cloud at the beginning. If

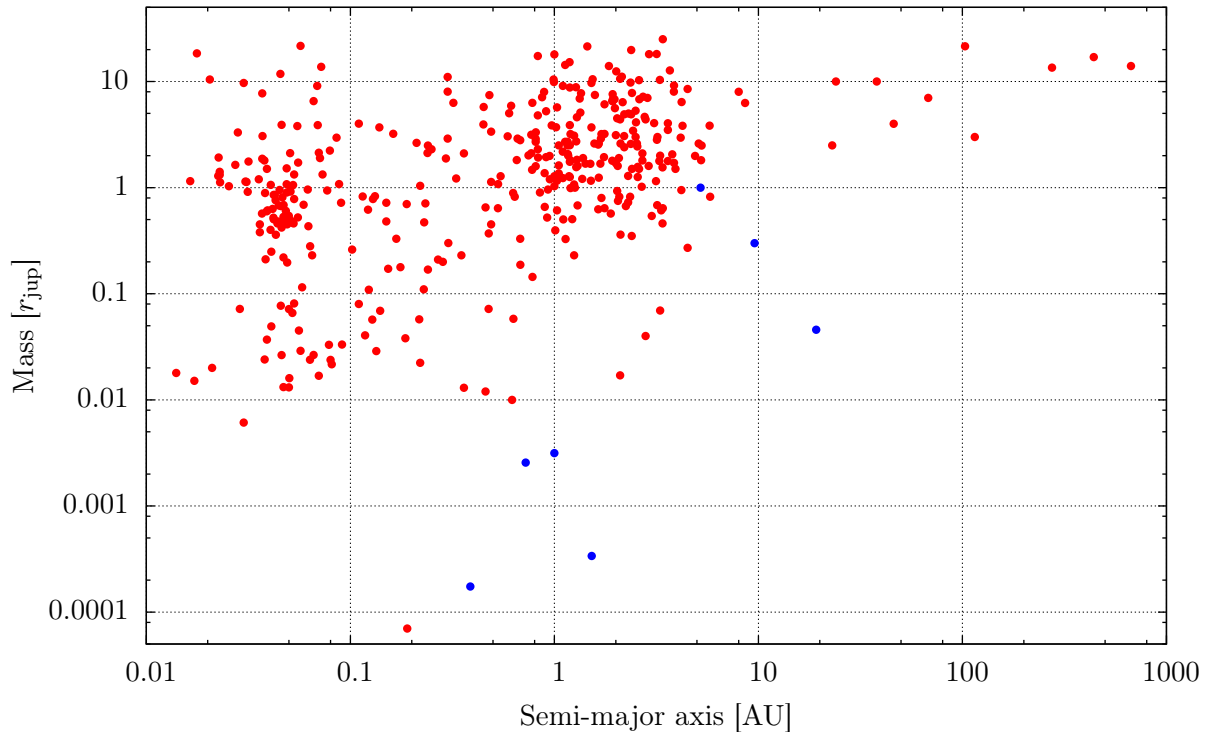


Figure 1.1: Distribution of extrasolar planets (red points) as of February 9th, 2010. The planets of the solar system (blue points) are displayed for comparison (www.exoplanet.eu)

the mass exceeds the Jeans limit (Jeans, 1902) it collapses and consequential temperature and pressure will increase dramatically. If density and temperature are high enough nuclear reactions can occur and a protostar is created. The rest of the molecular cloud, which is about 10 % to 0.1 % the mass of the original cloud, begins to collapse into a disk co-rotating the emerging star to conserve the angular momentum in the cloud. The vertical extent of the disk is ten to thirty times smaller than its horizontal extent. Usually, the disk's mass ranges from $10^{-3}M_{\star}$ to $10^{-1}M_{\star}$, but there have been detected more massive disks, for example in the Orion Nebula cluster (Eisner and Carpenter, 2006). Figure 1.2 shows pictures from disks in the Orion Nebula.

There are two competing theories, how planets form in these disk. The *core accretion model* or *sequential accretion scenario* shall be discussed first:

Although most of the mass in the disk is in a gaseous state (mainly hydrogen and helium), the solid component, which consists of dust grains with a size ranging from $0.1\text{ }\mu\text{m}$ to $1\text{ }\mu\text{m}$, contributes to the formation of planetesimals. By collisions between them, they grow to aggregates of centimeter to meter size.

The gas pressure near the disk mid-plane will normally decrease with increasing radius and

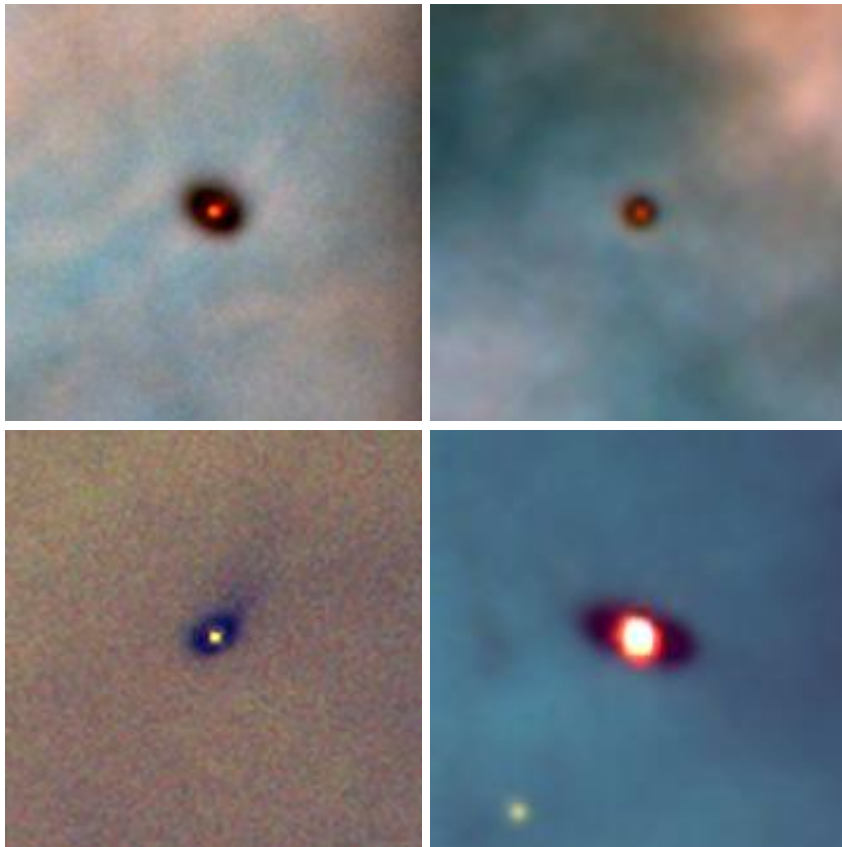


Figure 1.2: Hubble Space Telescope images of four protoplanetary disks around young stars in the Orion nebula, located 1.500 light-years away. Credit by Mark McCaughrean (Max-Planck-Institute for Astronomy), C. Robert O'Dell (Rice University), and NASA

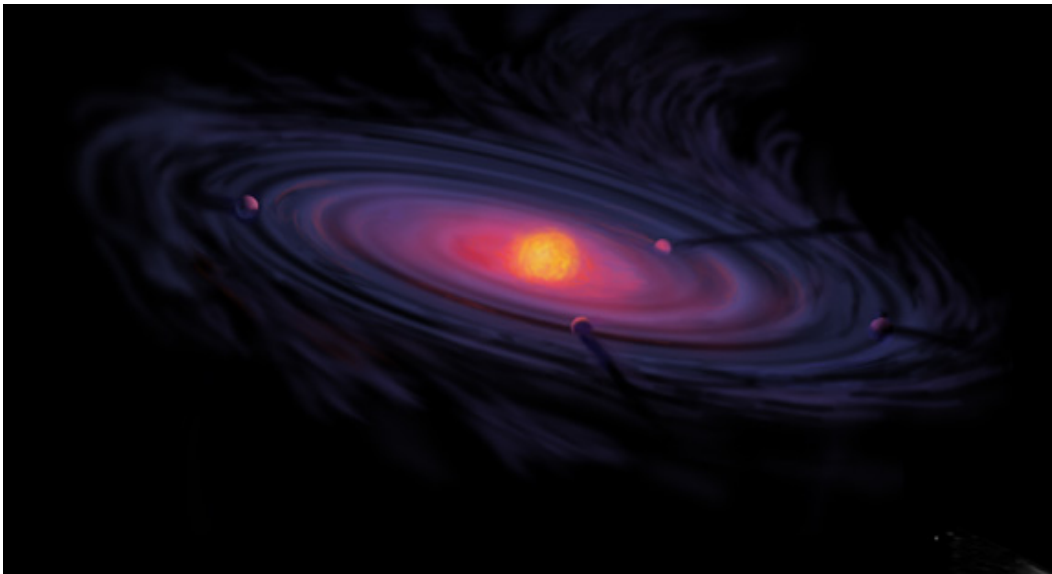


Figure 1.3: Artist's concept of a protoplanetary disk, NASA

therefore an outward pressure gradient will cause the gas to orbit with sub-Keplerian velocities. As the solid particles do not feel the gas pressure, they orbit at Keplerian velocity. This difference in velocity creates a drag force that will cause the solid particles to spiral inward toward the central star as they lose angular momentum (Weidenschilling, 1977). The velocity for particles with size within centimeter to meter range can be as high as 10^4 cm/s, so these particles could reach the central star before they decouple from this disk gas and are able to form kilometer size objects.

The solution for this issue is still unclear. Therefore different approaches are discussed. If there are any regions in the disk that have local pressure extrema, these could trap particles and stop them from migrating further inward (Haghighipour and Boss, 2003b,a). Klahr and Bodenheimer (2003) for example suggest vortices, formed by a baroclinic instability, or spiral-arms structures, formed by self-gravitating disks, which are density and pressure maxima.

Assuming that sufficiently massive planetesimals have been formed, these rocky cores start to accrete a gaseous envelope (Bodenheimer and Pollack, 1986; Pollack *et al.*, 1996) and then grow to gas giants with masses of Jupiter. Figure 1.3 shows an artist's concept of such a disk where some planetesimals or planets have formed already.

These gas giants will usually migrate inwards while accreting gas until most of the gas in disk is either accreted or dissipated. Figure 1.1 shows planets at very large radii (> 10 AU) that are very massive ($m > M_{\text{jup}}$) and thus are very unlikely to have been formed by core accretion, as they would migrate faster inwards than they could accrete enough mass (Nelson *et al.*, 2000; Bate *et al.*, 2003). Moreover, the formation timescale of such massive planets would exceed the disk's lifetime of a few millions years (Bally *et al.*, 1998; Haisch *et al.*, 2001; Briceño *et al.*, 2001; Eisner and Carpenter, 2003) by magnitudes.

Another theory to address these issues is the *disk instability theory*.

In this model, planets form directly by gravitational instability of overdense clumps in the

disk. Therefore the disk must be sufficiently massive. There is strong theoretical (Yorke and Bodenheimer, 1999) and observational (Osorio *et al.*, 2003; Rodríguez *et al.*, 2005; Eisner *et al.*, 2005) evidence that such disk do exists.

One of the main advantage of this theory is the fact, that the formation of gas giants is possible even in the shortest-lived protoplanetary disks and therefore the idea of disk instability or a hybrid theory where core accretion is accelerated by gravitational instabilities might be required to form some of the found gas planets. Especially planets with very large radii and high masses, such as found in figure 1.1 on the right hand side, are very likely to be formed by gravitational instabilities, whereas planets with very small radii are difficult to form because the disk have to cool down very fast.

This is still an inconsistency within this theory. It is unclear, if the disk can cool sufficiently fast, so that compression energy can be radiated away. This is one point we are addressing in this thesis. We therefore used local radiative cooling to cool down the disk in our simulations.

A more detailed overview of the disk instability theory can be found in Durisen *et al.* (2007).

1.2 Outline

In Section 2 we want to introduce the theoretical background of this thesis and explain the equations used in the code.

Section 3 then focuses on the implementation of these equations in the `FARGO` code.

Afterwards we present our results in section 4.

Section 5 gives a brief summary of the work done.

1.3 Notations

Throughout this work, we used the centimetre-gram-second (cgs) unit system and constants listed in table 1.1.

Table 1.1: Physical constants used throughout this work.

gravitational constant	\mathcal{G}	$=$	$6.674 \cdot 10^{-8} \text{ cm}^3/\text{g s}^2$
astronomical unit	AU	$=$	$1.49597871475 \cdot 10^{13} \text{ cm}$
Jupiter semi-major axis	r_{jup}	$=$	$5.204267 \text{ AU} = 7.785472 \cdot 10^{13} \text{ cm}$
molecular mass	m_{μ}	$=$	$1.66053878283 \cdot 10^{-24} \text{ g}$
solar mass	M_{\odot}	$=$	$1.9884 \cdot 10^{33} \text{ g}$
Earth mass	M_{\oplus}	$=$	$3.0034896 \cdot 10^{-6} M_{\odot} = 5.9723 \cdot 10^{27} \text{ g}$
Jupiter mass	M_{jup}	$=$	$1.899 \cdot 10^{27} \text{ g}$
radiation constant	a	$=$	$\frac{4\sigma_R}{c} = 7.57 \cdot 10^{-15} \text{ erg/cm}^3 \text{ K}$
Boltzmann constant	k_B	$=$	$1.380650424 \cdot 10^{-16} \text{ erg/K}$
Planck constant	h	$=$	$6.6260689633 \cdot 10^{27} \text{ erg s}$
speed of light	c	$=$	$299792458 \cdot 10^2 \text{ cm/s}$
Stefan-Boltzmann constant	σ_R	$=$	$\frac{2\pi^5 k_B^4}{15h^3 c^2} = 5.6704 \cdot 10^{-5} \text{ erg/cm}^2 \text{ s K}^4$

2 Theoretical foundations

2.1 Accretion disks

In section 1 we described the framework of planet formation as accretion disks. While these disk's radial extent can reach a few hundreds of AU, its vertical extent is much smaller: Usually the disk's aspect ratio h , which is defined by $h = \frac{H}{r}$ where H is the vertical pressure scale height, ranges from 0.03 to 0.1. If the disk is in hydrostatic equilibrium in the vertical direction H can be written as

$$H = \frac{c_s}{\Omega} \quad (2.1)$$

where c_s is the local sound speed and Ω the angular rotation rate. As the material in the flat disk around the star rotates more or less Keplerian, the angular rotation rate is

$$\Omega \approx \Omega_K = \sqrt{\frac{\mathcal{G}M_\star}{r^3}} \quad (2.2)$$

The angular momentum of a the mass element m at a radius r is

$$J = m\sqrt{\mathcal{G}M_\star r} \quad (2.3)$$

as the gravitational field is nearly Keplerian. The energy of the mass element is given by

$$E = -\frac{1}{2} \frac{\mathcal{G}M_\star m}{r} \quad (2.4)$$

J diverges for $r \rightarrow \infty$ but E converges against zero for $r \rightarrow \infty$.

So, evolving the disk over time, most of the material will flow inward carrying mass towards the star whereas a very small part of the mass can swallow most or all of the angular momentum of the disk and carry it outwards. The star will then accrete the mass of the inner edge of the accretion disk. The typical accretion rate is from about $10^{-9}M_\odot/\text{yr}$ to $10^{-8}M_\odot/\text{yr}$. If we consider only molecular viscosity as a source for inward radial drift, it is orders of magnitude too small to account for this disk accretion rates. Therefore the inward drift of the gas is often modelled with an phenomenological approach for an effective viscosity proposed by [Shakura and Sunyaev \(1973\)](#), where the kinematic viscosity takes the form:

$$\nu = \alpha c_s H = \alpha H^2 \Omega_K = \alpha c_s^2 \Omega_K^{-1} \quad (2.5)$$

with c_s the local sound speed and α a numerical constant ranging typically from 10^{-5} to 10^{-1} . The last two steps used equation 2.1.

More background on accretion disks, can be found in [Binney and Tremaine \(1987\)](#); [Pringle \(1981\)](#).

2.2 Hydrodynamics

2.2.1 Basic equations

Hydrodynamics consists of three basic equations, which are all based on three basic principles:

- Mass is neither created nor destroyed (conservation of mass)
- Change of momentum results from external forces (conservation of momentum)
- Energy is neither created nor destroyed (conservation of energy)

Coming from these basic principles, it's possible to determine the basic equation.

The first equation results from the conservation of mass and is called continuity equation:

$$\frac{\partial \rho}{\partial t} + \nabla \cdot (\rho \vec{v}) = 0 \quad (2.6)$$

Where ρ is the mass density and \vec{v} the velocity meaning that the temporal change of density of mass density in a volume is caused by change of mass flux through the volume.

The second equation includes the pressure p , caused by thermal movement of gas particles and follows from the conservation of momentum.

$$\rho \left(\frac{\partial \vec{v}}{\partial t} + (\vec{v} \cdot \nabla) \vec{v} \right) = -\nabla p + \rho \vec{f} \quad (2.7)$$

As additional forces, such as gravitation, Coriolis force and centrifugal force, can change the momentum of the gas, the specific external force \vec{f} appears as a source term in the equation. External forces \vec{F} relates to \vec{f} through

$$\vec{F} = \int \rho \vec{f} dV \quad (2.8)$$

The third equation covers the conservation of energy and includes the change of thermal energy of adiabatic changes of the system.

$$\frac{\partial(\rho\epsilon)}{\partial t} + \nabla \cdot (\rho\epsilon\vec{v}) = -p\nabla \cdot \vec{v} \quad (2.9)$$

The specific energy ϵ is defined analogue to 2.8.

The set of equations 2.6, 2.7 and 2.9 are often called *Euler equations* whereas equation 2.7 is known as the *Euler equation*. The Euler equations are the basic equations of motion for ideal fluids and are often completed with a equation of state for the pressure p .

More information about the derivation of the Euler equations can be found in Kley (2008b).

2.2.2 Viscosity

The Euler equations described in 2.2.1 cover only ideal fluids and so dissipative effects like viscosity or heat conduction are not covered.

Equation 2.7 only takes pressure forces which are perpendicular to the surface into account. If there are particles carrying momentum from one to another volume friction appears. So the total force on the surface of a volume can be described as

$$\vec{F} = \oint_{\partial V} (-p\hat{n} + \sigma\hat{n}) df \quad (2.10)$$

where $p\hat{n}$ is the pressure force as seen before. \hat{n} is the surface normal and σ the stress tensor.

Usually one makes the following, phenomenological motivated, demands on σ :

- σ is symmetric (conservation of angular momentum)
- σ is invariant to translation and rotation
- σ depends only linear on the first derivation of velocity (linear approximation)

The most general form of a second-order tensor which meets the requirements is

$$\sigma_{ij} = \eta \left(\frac{\partial v_i}{\partial x_j} + \frac{\partial v_j}{\partial x_i} \right) + \lambda (\nabla \vec{v}) \delta_{ij} \quad (2.11)$$

where δ_{ij} is the Kronecker delta (Mihalas and Weibel-Mihalas, 1999, §25). η and λ are scalar quantities for Newtonian fluids which depend on p and T in general. Usually σ is written in the following form

$$\sigma_{ij} = 2\eta \left[\frac{1}{2} \left(\frac{\partial v_i}{\partial x_j} + \frac{\partial v_j}{\partial x_i} \right) - \frac{1}{3} (\nabla \vec{v}) \delta_{ij} \right] + \zeta (\nabla \vec{v}) \delta_{ij} \quad (2.12)$$

where η is called shear viscosity and ζ volume viscosity (also called bulk or second viscosity).

If this viscous forces are taken in into account, equation 2.7 changes to

$$\rho \left(\frac{\partial \vec{v}}{\partial t} + (\vec{v} \cdot \nabla) \vec{v} \right) = -\nabla p + \rho \vec{f} + \nabla \cdot \sigma \quad (2.13)$$

This equation is called *Navier-Stokes equation*.

Equation 2.9 has also be modified to include the heat generated by the viscosity:

$$\frac{\partial(\rho\epsilon)}{\partial t} + \nabla(\rho\epsilon\vec{v}) = -p\nabla\vec{v} + (\sigma \cdot \nabla)\vec{v} \quad (2.14)$$

2.2.3 Heat transport

Equation 2.9 rests upon the assumption of conservation of energy, so energy is neither created nor destroyed. But if we consider only a sub-part of a total system, energy can be lost by heat conduction. So, we need to add a source term for external energy flux \vec{F} :

$$\frac{\partial(\rho\epsilon)}{\partial t} + \nabla(\rho\epsilon\vec{v}) = -p\nabla\vec{v} + (\sigma \cdot \nabla)\vec{v} - \nabla\vec{F} \quad (2.15)$$

The set of equations 2.6, 2.13 and 2.15 are often called *Navier-Stokes equations*.

Usually the external energy flux \vec{F} is given by

$$\vec{F} = \vec{F}_{\text{cond}} + \vec{F}_{\text{rad}} \quad (2.16)$$

where \vec{F}_{cond} is the energy flux caused by conduction and \vec{F}_{rad} is the energy flux caused by radiation.

According to Fourier's law, the heat conduction term can be written as

$$\vec{F}_{\text{cond}} = -k\nabla T \quad (2.17)$$

where k is the thermal conductivity.

In local thermal equilibrium the radiation term can be written as

$$\vec{F}_{\text{rad}} = -\frac{4}{3} \frac{ca}{\kappa_R \rho} T^3 \nabla T = -\frac{16}{3} \frac{\sigma_R}{\kappa_R \rho} T^3 \nabla T \quad (2.18)$$

where $a = \frac{4\sigma_R}{c}$ is the radiation constant, κ_R the Rosseland mean opacity and $\sigma_R = \frac{2\pi^5 k_B^4}{15h^3 c^2}$ the Stefan-Boltzmann constant. The Rosseland mean opacity κ_R is defined by

$$\frac{1}{\kappa_R} \int_0^\infty \frac{\partial u(\nu, T)}{\partial T} d\nu = \int_0^\infty \frac{1}{\kappa(\nu)} \frac{\partial u(\nu, T)}{\partial T} d\nu \quad (2.19)$$

where κ is the frequency dependent opacity and $u(\nu, T)$ follows from Planck's law:

$$u(\nu, T) = \frac{8\pi h \nu^3}{c^3} \frac{1}{e^{\frac{h\nu}{k_B T}} - 1} \quad (2.20)$$

2.3 Self-gravity

As the disk is spatially spread, gravity plays an important role. The gravity acting on the disk by its own gravitational potential is called self-gravity. The gravitational potential at a point \vec{r} is

$$\Psi(\vec{r}) = -\mathcal{G} \int_V \frac{\rho(\vec{r}')}{|\vec{r} - \vec{r}'|} d\vec{r}' \quad (2.21)$$

To include self-gravity into the hydrodynamics equations, it has to be added as an additional external force in equation 2.13. Including self-gravity can destabilize the disk and possibly lead to fragmentation. As we plan to study the possibility of planet fragmentation through gravitational instabilities we present in the following the stability analysis of a flat disk.

We now assume a disk of infinitesimal thickness in which the volume density ρ , has the form $\rho = \Sigma(r, \varphi) \delta(z)$. If we now integrate the equations 2.6 and 2.7 over all z we obtain the two-dimensional Euler-equation:

$$\frac{\partial \Sigma}{\partial t} + \nabla \cdot (\Sigma \vec{v}) = 0 \quad (2.22)$$

$$\frac{\partial (\Sigma v_r)}{\partial t} + \nabla \cdot (\Sigma v_r \vec{v}) = \Sigma r \Omega^2 - \frac{\partial p}{\partial r} - \Sigma \frac{\partial \Psi}{\partial r} \quad (2.23)$$

$$\frac{\partial (\Sigma r^2 \Omega)}{\partial t} + \nabla \cdot (\Sigma r^2 \Omega \vec{v}) = -\frac{\partial p}{\partial \varphi} - \Sigma \frac{\partial \Psi}{\partial \varphi} \quad (2.24)$$

where $\vec{v} = (v_r, v_\varphi) = (v_r, r\Omega)$, p is the vertically integrated pressure and Ψ the gravitational potential which satisfies Poisson's equation which reads now in (r, φ) -coordinates:

$$\frac{1}{r} \frac{\partial}{\partial r} \left(r \frac{\partial \Psi}{\partial r} \right) + \frac{1}{r^2} \frac{\partial^2 \Psi}{\partial \varphi^2} + \frac{\partial^2 \Psi}{\partial z^2} = 4\pi \mathcal{G} \Sigma \delta(z) \quad (2.25)$$

We now assume linear perturbations about the axisymmetric equilibrium state in the plane where $z = 0$, where all quantities $f \in \{\Omega, v_r, \Sigma, P, \Psi\}$ are of the form $f = f_0(r) + f_1(r, \varphi, t)$. f_1 can be written as $\tilde{f}_1(r) e^{-i\sigma t + im\varphi}$ and if we substitute this in the linearized perturbation equations of 2.22, 2.23 and 2.24, we obtain

$$\tilde{\Sigma}_1(\sigma - m\Omega_0) = -i\Sigma_0 \tilde{v}'_{r1} + \Sigma_0 m \tilde{\Omega}_1 \quad (2.26)$$

$$\tilde{v}_{r1}(\sigma - m\Omega_0) = -i2r\Omega_0 \tilde{\Omega}_1 - i \frac{c_{s0}^2}{\Sigma_0} \tilde{\Sigma}'_1 - i \tilde{\Psi}'_1 \quad (2.27)$$

$$\tilde{\Omega}_1(\sigma - m\Omega_0) = -i \frac{\kappa_0^2}{2r\Omega_0} \tilde{v}_{r1} - \frac{c_{s0}^2}{\Sigma_0} im \tilde{\Sigma}_1 + \frac{1}{r^2} im \tilde{\Psi}_1 \quad (2.28)$$

where $\kappa_0^2 = \frac{2\Omega_0}{r} \frac{\partial}{\partial r}(r^2\Omega_0)$ is the epicyclic frequency and $c_{s0} = \sqrt{\frac{\gamma p_0}{\Sigma_0}}$ is the sound speed.

If we set the radial dependency of $\tilde{f}_1(r)$ to $\propto e^{ikr}$ and we assume tight winding ($kr \gg m$) (Binney and Tremaine, 1987, section 6.2.2) the equations simplify to

$$\tilde{\Sigma}_1(\sigma - m\Omega_0) = k\Sigma_0 \tilde{v}_{r1} \quad (2.29)$$

$$\tilde{v}_{r1}(\sigma - m\Omega_0) = -i2r\Omega_0 \tilde{\Omega}_1 + \frac{c_{s0}^2}{\Sigma_0} k \tilde{\Sigma}_1 + k \tilde{\Psi}_1 \quad (2.30)$$

$$\tilde{\Omega}_1(\sigma - m\Omega_0) = -i \frac{\kappa_0^2}{2r\Omega_0} \tilde{v}_{r1} \quad (2.31)$$

For the gravitational potential Ψ we do the same approximations to 2.25 and obtain

$$\tilde{\Psi}_1 = \frac{2\pi \mathcal{G} \tilde{\Sigma}_1}{|k|} \quad (2.32)$$

The substitution of equation 2.29, 2.31 and 2.32 in 2.30 leads to the dispersion relation:

$$(\sigma - m\Omega_0)^2 = \kappa_0^2 + c_{s0}^2 - 2\pi \mathcal{G} |k| \Sigma_0 \quad (2.33)$$

We now get stability ($\sigma^2 > 0$) for axisymmetric perturbations ($m = 0$) when the right-hand side of equation 2.33 is positive. It follows that

$$\zeta^2 - \zeta + \frac{Q}{4} \geq 0 \quad (2.34)$$

where Q is Toomre's stability parameter (Toomre, 1964) and $\zeta = \frac{k_T}{|k|}$ is the wave number $|k|$ in units of the Toomre wave number scale k_T :

$$Q = \frac{\kappa_0 c_{s0}}{\pi \mathcal{G} \Sigma_0} \quad (2.35)$$

$$k_T = \frac{\kappa_0^2}{2\pi \mathcal{G} \Sigma_0} = \frac{\kappa_0}{2c_{s0}} Q \quad (2.36)$$

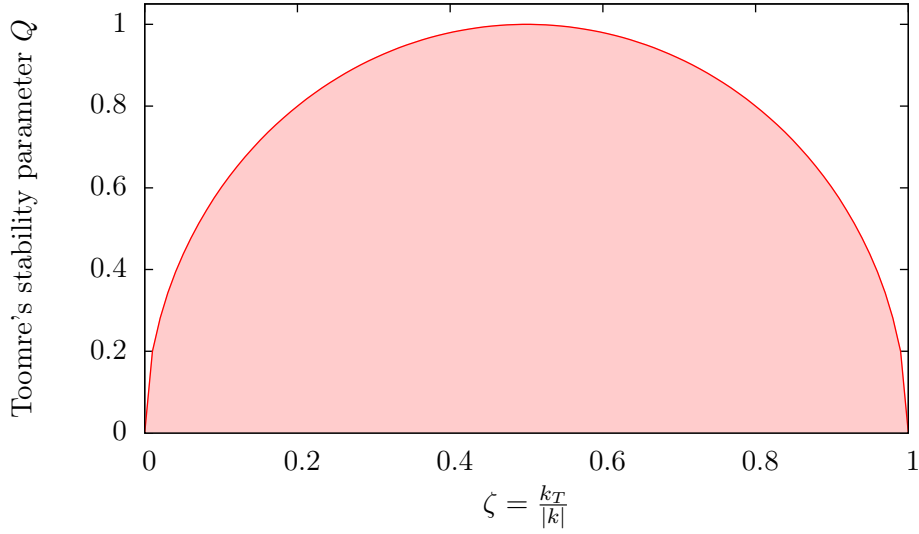


Figure 2.1: Stability diagram for clumping into axisymmetric rings by a self-gravitating differentially rotating, gaseous disk. The lighter red area is the unstable region and the red curve shows marginal stability. The white area is stable. Short-wavelength disturbances are stabilized by the effects of pressure whereas long-wavelength disturbances are stabilized by the effects of rotation.

Figure 2.1 illustrates equation 2.34. The lighter red area shows where the disk is unstable and the red curve shows marginal stability. So the disk is for $Q \geq 1$ stable and for $Q < 1$ it depends on the wave number $|k|$ and if it's stabilized either by pressure (short wave disturbances) or rotation (long wave disturbances).

Further discussion on stability can be found in Kley (2008a); Shu (1992); Binney and Tremaine (1987). Papaloizou and Savonije (1991) showed that for non-axisymmetric disturbances, which grow as multi-armed spirals, the disks becomes unstable for $Q \lesssim 1.5$.

2.4 Thermodynamics

Disk evolution heavily depends on the thermodynamics within in the disk. As the material is compressed when the disks collapses additional internal energy is generated. This heats up the disk and affects the further disk evolution. Therefore the consideration of thermodynamics is very important.

Many simulations of accretion disk only use an isothermal disk model, where the temperature is constant over time. As we include viscous heating and radiative cooling, we need are more realistic treatment of thermodynamics.

As the gas in the accretion disk is is nearly ideal (it is primarily composed of H_2 molecules) we use an ideal gas law to connect the pressure p with the surface density Σ and the temperature T :

$$p = \mathcal{R}\Sigma T \quad (2.37)$$

where \mathcal{R} is a constant, equal to the universal gas constant divided by the mean molecular

mass μm_μ with m_μ the molecular mass and $\mu = 2.35$ for a typical accretion disk with about 70% hydrogen and 30% helium. \mathcal{R} is equal to unity in code units (see section 3.1.2).

We assume an ideal gas where the specific heat at constant volume $c_v = \left(\frac{\partial \epsilon}{\partial T}\right)_V$ is constant, and therefore the specific thermal energy

$$\epsilon(T) = \int_0^T c_v dT' = c_v T + \underbrace{\epsilon(0)}_{:=0} = c_v T \quad (2.38)$$

scales with the temperature T . If h is the specific enthalpy and we further assume that the specific heat at constant pressure $c_p = \left(\frac{\partial h}{\partial T}\right)_V$ is also constant, we can write

$$h(T) = \int_0^T c_p dT' = c_p T + \underbrace{\epsilon(0)}_{:=0} = c_p T \quad (2.39)$$

If we now consider the first law of thermodynamics and use the definition of the specific enthalpy $h = \epsilon + p\Sigma$, we can find the relation (Kley, 2008b, section 1.1)

$$c_p - c_v = \mathcal{R} \quad (2.40)$$

We define the specific heat ratio (adiabatic index) as

$$\gamma := \frac{c_p}{c_v} = 1 + \frac{\mathcal{R}}{c_v} \quad (2.41)$$

If we define the thermal energy per unit area $e = \epsilon\Sigma$ equation 2.37 and 2.41 can be combined as

$$p = \mathcal{R}\Sigma T = (\gamma - 1)c_v T\Sigma = (\gamma - 1)e \quad (2.42)$$

The specific entropy $s = s_0 + c_v \ln \frac{p}{\Sigma^\gamma}$ stays constant for adiabatic changes of state ($ds = 0$) can be inverted to

$$p = \exp\left(\frac{s - s_0}{c_v}\right) \Sigma^\gamma = \kappa(s) \Sigma^\gamma \quad (2.43)$$

Together with the definition of the local sound speed c_s we get

$$c_s^2 = \left(\frac{\partial p}{\partial \Sigma}\right)_s = \frac{\gamma p}{\Sigma} = \gamma \mathcal{R} T \quad (2.44)$$

as a simple expression for the local sound speed which defines the viscosity ν in the α -model (see equation 2.5). Further details on the connection of the thermodynamical quantities can be found in Kley (2008b); Baruteau (2008).

2.4.1 Estimation of cooling

As already stated, compression (e.g. by gravitational instabilities) heats up the disk, and this energy has to be radiated way fast enough to allow further compression by gravitation as the

thermal pressure has to be overcome (Gammie, 2001). The time needed to cool the disk can be measured in the local cooling time τ_{cool} which is defined by

$$\frac{de}{dt} = -\frac{e}{\tau_{\text{cool}}} \quad (2.45)$$

Several theoretical and numerical studies (Gammie, 2001; Johnson and Gammie, 2003; Rice *et al.*, 2003, 2005; Mayer *et al.*, 2004; Mejía *et al.*, 2005) indicate that for disc fragmentation to occur the cooling time τ_{cool} must satisfy

$$\tau_{\text{cool}} < \beta(\gamma) \Omega^{-1} \quad (2.46)$$

where

$$0.5 \lesssim \beta(\gamma) \lesssim 2.0 \quad (2.47)$$

This means that cooling has to occur on orbital timescales.

If we examine equation 2.15 in the hydrostatic and thermal equilibrium we find that

$$0 = (\sigma \cdot \nabla) \vec{v} - \nabla \cdot \vec{F} \equiv Q_+ - Q_- \quad (2.48)$$

The heating term Q_+ (viscous dissipation) can be written as

$$Q_+ = \frac{1}{2\nu\Sigma} [\sigma_{rr}^2 + 2\sigma_{r\varphi}^2 + \sigma_{\varphi\varphi}^2] + \frac{2\nu\Sigma}{9} (\nabla \cdot \vec{v})^2 \quad (2.49)$$

where σ is the viscous stress tensor (see equation 2.12) in polar coordinates. The term is dominated by the $r\varphi$ -component and thus

$$Q_+ \approx \frac{1}{2\nu\Sigma} 2\sigma_{r\varphi}^2 = \frac{1}{\nu\Sigma} \left[\nu\Sigma \left(r \frac{\partial}{\partial r} \frac{v_\varphi}{r} + \frac{1}{r} \frac{\partial v_r}{\partial \varphi} \right) \right]^2 \quad (2.50)$$

$$\approx \nu\Sigma r^2 \left(\frac{\partial}{\partial r} \Omega \right)^2 \approx \nu\Sigma r^2 \left(\frac{\partial}{\partial r} \Omega_K \right)^2 \quad (2.51)$$

$$= \nu\Sigma \frac{9}{4} \Omega_K^2 \quad (2.52)$$

where we used in the third step that $\frac{\partial v_r}{\partial \varphi} = 0$ in equilibrium and $\Omega \approx \Omega_K$.

We can now introduce a simple β -Cooling by

$$Q_- = \frac{\Omega_K}{\beta} e = \frac{\Omega_K}{\beta} \Sigma c_v T \quad (2.53)$$

If we now substitute the terms for Q_+ and Q_- in equation 2.48 we obtain

$$\nu\Sigma \frac{9}{4} \Omega_K^2 = \frac{\Sigma c_v T}{\beta} \Omega_K \quad (2.54)$$

If we now use the definition of ν in the α -model and used the thermodynamical relations we derived earlier, we find after some algebra (Gammie, 2001):

$$\beta = \frac{4}{9} \frac{1}{\gamma(\gamma-1)} \frac{1}{\alpha} \quad (2.55)$$

So in equilibrium there is a connection between the local cooling timescale τ_{cool} and the α of the viscosity. If α and β do not match, the equilibrium must be unstable.

Apart from this systematic problem with β -cooling it is also very unphysical as cooling does not depend on any local factors like density or temperature. We therefore introduce a more realistic cooling based on local opacities in section [3.8](#).

3 Numerical methods

3.1 Introduction - FARGO

In this thesis, we used the **FARGO** code written by [Masset \(2000\)](#). **FARGO** is a two-dimensional hydrodynamical grid code which solves the isothermal Navier-Stokes equations using a staggered polar grid (see [3.3](#)). To speed up calculations the code uses the FARGO-Algorithm described in section [3.4](#). The original version can be found on <http://fargo.in2p3.fr>.

The standard version of the **FARGO** code has no support for self-gravity or an energy equation. Self-gravity and basic energy-equation support has been added by Clément Baruteau in his PhD thesis ([Baruteau, 2008](#)).

The **FARGO** code is fully parallelized using the Message Passing Interface Standard¹ (MPI) and therefore can run on either multicore systems or clusters. To run on multiple cores the grid is split radially in several rings and then each part is calculated independently on a core (domain decomposition). After each time-step some overlapping area is synchronized between the cores which calculated neighbour areas.

3.1.1 2D quantities

As **FARGO** is a two-dimensional code, all quantities have to be reduced to two dimensions. For example the volume density ρ is reduced to a surface density Σ by

$$\Sigma = \int_{-\infty}^{\infty} \rho_0 \cdot e^{-\frac{z^2}{2H^2}} dz = \sqrt{2\pi} \rho_0 H = \sqrt{2\pi} \rho_0 h r \quad (3.1)$$

assuming that ρ is vertically a Gauss-profile. H is the vertical height of the disk, where as $h = \frac{H}{r}$ is the aspect ratio.

In most of our simulations we used

$$\Sigma = 2\rho_0 h r \quad (3.2)$$

to allow comparison with results from other studies which used this simplified relation.

3.1.2 Code units

To optimize the value range of data-types (like double) and for simplification of equations the code uses special code units, instead of using the centimetre-gram-second (cgs) or metre-kilogram-second (mks) system.

The code units are defined by

- A planet with an orbital radius l_0 has an orbital period of 2π .
- The central mass has the mass m_0 .

All other units are derived from this definition. In particularly it applies:

¹<http://www.mcs.anl.gov/research/projects/mpi/standard.html>

- The time unit t_0 is $\sqrt{\frac{l_0^3}{\mathcal{G}m_0}}$
- The gravitational constant \mathcal{G} is equal 1.
- The temperature unit T_0 is $\sqrt{\frac{\mathcal{G}m_0}{Rl_0}}$
- The gas constant divided by the mean molecular mass \mathcal{R} is equal to 1.

3.2 Finite differences

FARGO solves the fluid equation using the method of finite-differences with a time-explicit, multistep solution procedure. Therefore the solution of the partial differential equations is split into parts using operator splitting. For a given operator operator $\mathcal{L}(y)$, e.g. given by

$$\mathcal{L}(y) = \frac{\partial y}{\partial t} \quad (3.3)$$

the operator is split into $\mathcal{L}(y) = \mathcal{L}_1(y) + \mathcal{L}_2(y) + \dots$ and then the solution procedure reads as

$$\frac{y^1 - y^0}{\Delta t} = L_1(y^0) \quad (3.4)$$

$$\frac{y^2 - y^1}{\Delta t} = L_2(y^1) \quad (3.5)$$

$$\frac{y^3 - y^2}{\Delta t} = \dots \quad (3.6)$$

where L_i are the finite-difference representations of the operators \mathcal{L}_i . The solution obtained via the split method is of course an approximation to the correct solution of the full nonlinear, multidimensional operator \mathcal{L} , but numerical experiments have shown that such a multistep algorithm is more accurate than a single integration step base on old data ([Hawley et al., 1984](#)).

In equation 3.4 we already used the finite-difference scheme, which means that we use finite differences to approximate derivatives. For example, if want to calculate the derivative with respect to x from a quantity ξ on the position i of our discrete grid, we can approximate

$$\frac{\partial \xi_i}{\partial x} \approx \frac{\xi_i - \xi_{i+1}}{x_i - x_{i+1}} = \frac{\xi_i - \xi_{i+1}}{-\Delta x_{i+1}} \quad (3.7)$$

$$\frac{\partial \xi_i}{\partial x} \approx \frac{\xi_i - \xi_{i-1}}{x_i - x_{i-1}} = \frac{\xi_i - \xi_{i-1}}{\Delta x_i} \quad (3.8)$$

where $\Delta x_i = x_i - x_{i-1}$. The first equation is an approximation using right-side differences whereas the second equation uses left-side differences. These are both approximations of first-order.

To improve the approximation and get rid of the favoritism of one direction **FARGO** uses centered-differences of second order. Here the approximation read as

$$\frac{\partial \xi_i}{\partial x} \approx \frac{\xi_{i+1} - \xi_{i-1}}{x_{i+1} - x_{i-1}} = \frac{\xi_{i+1} - \xi_{i-1}}{\Delta x_i + \Delta x_{i+1}} = \frac{\xi_{i+1} - \xi_{i-1}}{2\Delta x} \quad (3.9)$$

where we used $\Delta x = \Delta x_i$ when the grid is evenly spaced.

In **FARGO** the Navier-Stokes equations discussed in section 2.2 are now split into two steps, called the source and the transport steps, using operator splitting. In the source step, we solve finite-difference approximations to

$$\frac{\partial v_r}{\partial t} = \frac{v_\varphi^2}{r} - \frac{1}{\Sigma} \frac{\partial p}{\partial r} - \frac{\partial \Psi}{\partial r} + \frac{1}{r\Sigma} \left[\frac{\partial}{\partial r} (r\sigma_{rr} + \frac{\partial}{\partial \varphi} \sigma_{r\varphi} - \sigma_{\varphi\varphi}) \right] + \frac{1}{\Sigma} \frac{\partial q_r}{\partial r} \quad (3.10)$$

$$\frac{\partial v_\varphi}{\partial t} = -\frac{1}{\Sigma} \frac{1}{r} \frac{\partial p}{\partial \varphi} - \frac{1}{r} \frac{\partial \Psi}{\partial \varphi} + \frac{1}{r\Sigma} \left[\frac{\partial}{\partial r} (r\sigma_{r\varphi}) + \frac{\partial}{\partial \varphi} \sigma_{\varphi\varphi} + \sigma_{r\varphi} \right] - \frac{1}{\Sigma} \frac{1}{r} \frac{\partial q_\varphi}{\partial \varphi} \quad (3.11)$$

where q_r and q_φ are components of an artificial viscous pressure, required to smooth shocks on a staggered-mesh code (see section 3.3) and are given by

$$q_r = \begin{cases} C_{\text{VNR}}^2 \Sigma \left(\frac{\partial v_r}{\partial r} \Delta r \right)^2 & \left(\frac{\partial v_r}{\partial r} \Delta r \right) < 0 \\ 0 & \text{otherwise} \end{cases} \quad (3.12)$$

$$q_\varphi = \begin{cases} C_{\text{VNR}}^2 \Sigma \left(\frac{\partial v_\varphi}{\partial \varphi} r \Delta \varphi \right)^2 & \left(\frac{\partial v_\varphi}{\partial \varphi} r \Delta \varphi \right) < 0 \\ 0 & \text{otherwise} \end{cases} \quad (3.13)$$

C_{VNR}^2 is the Neumann-Richtmyer's constant (Stone and Norman, 1992; Masset, 2000) and Δr and $r\Delta\varphi$ are the sizes of the mesh.

The transport step accounts for the fluid advection by solving finite-difference approximations to the equations

$$\frac{\partial \Sigma}{\partial t} + \nabla \cdot (\Sigma \vec{v}) = 0 \quad (3.14)$$

$$\frac{\partial \Sigma v_r}{\partial t} + \nabla \cdot (\Sigma v_r \vec{v}) = 0 \quad (3.15)$$

$$\frac{\partial r \Sigma v_\varphi}{\partial t} + \nabla \cdot (r \Sigma v_\varphi \vec{v}) = 0 \quad (3.16)$$

These equations can now be rewritten as

$$\iiint \frac{\partial}{\partial t} \begin{pmatrix} \Sigma \\ \Sigma v_r \\ r \Sigma v_\varphi \end{pmatrix} dV = \iiint \begin{pmatrix} \nabla \cdot (\Sigma \vec{v}) \\ \nabla \cdot (\Sigma v_r \vec{v}) \\ \nabla \cdot (r \Sigma v_\varphi \vec{v}) \end{pmatrix} dV = \oint \begin{pmatrix} \Sigma \vec{v} \\ \Sigma v_r \vec{v} \\ r \Sigma v_\varphi \vec{v} \end{pmatrix} d\vec{S} \quad (3.17)$$

where we used Gauss' theorem in the last step. Thus, all quantities can be updated by taking into account their fluxes at each cell interface. This is now be done using a simple second-order upwind interpolation (van Leer, 1977) individually for each direction. The φ -direction is handled in a special way in **FARGO** (see section 3.4).

More details on the implementation of finite-differences in **FARGO** can be found in Baruteau (2008) and for more detailed information on finite-differences in two-dimensional hydro-codes, in particular the **ZEUS** code on which **FARGO** is based, see Stone and Norman (1992).

3.3 Staggered grid

As **FARGO** uses centered differences, odd-even decoupling can appear. Odd-even decoupling is an undesired effect of discretization that leads to checker board patterns in the solution. To avoid this, a staggered grid is used in **FARGO**.

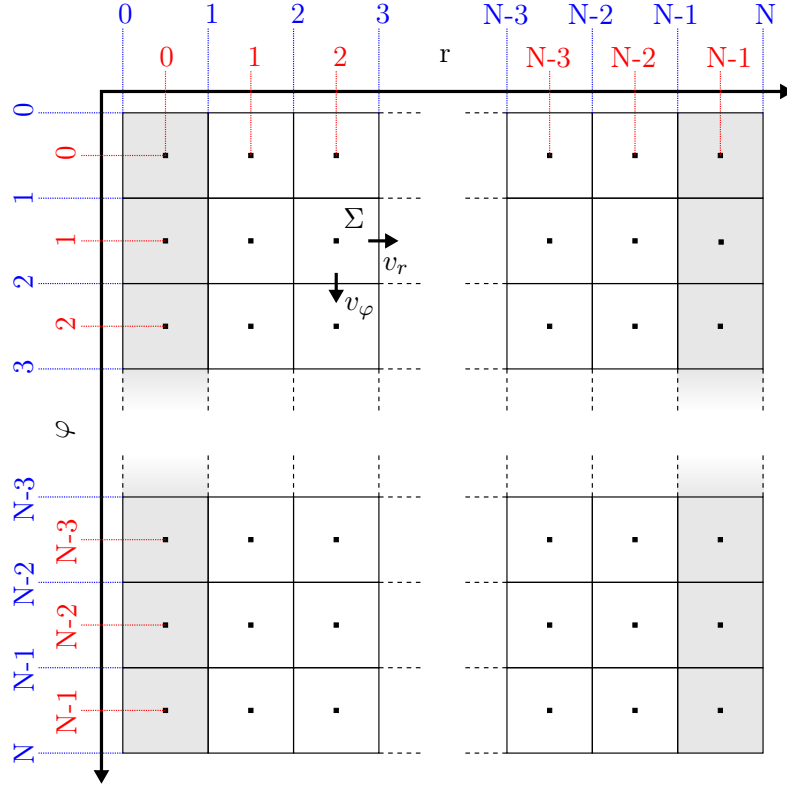


Figure 3.1: Schematic of staggered grid used in **FARGO**. The gray cells represent the ghost cells used in radial direction (see section 3.5) whereas the white cells represent the active cells on which calculations are done. Scalar quantities are stored cell centered (dots) as vector quantities are stored on the cell borders (arrows).

A staggered grid stores all scalar variables like density, energy, etc. cell-centered whereas all vector variables like velocity are located at the cell faces. As each cell has only one center, but two sides in each direction and these sides are shared with the neighbors cells, there are in total $N - 1$ cell centers, but N cell borders for a grid with $N - 1$ cells.

Figure 3.1 illustrates the grid used in **FARGO**:

- Scalar quantities like density Σ are stored cell centered. This is illustrated as the red grid.
- Vector quantities like velocity v_φ and v_r are stored on the cell borders. This is illustrated as the blue grid.
- The gray cells are the ghost cells in radial direction, which are updated by the boundary condition after each time-step.
- There are no ghost cells in azimuthal direction, as the grid is periodical.

3.4 The FARGO Algorithm

When solving hyperbolic partial differential equations (PDEs) the time-step Δt is limited by

$$\Delta t_{ij} < C \cdot \min \left\{ \frac{\Delta r_{ij}}{v_{ij}^r}, \frac{r_{ij} \Delta \varphi_{ij}}{v_{ij}^\varphi}, \dots \right\} \quad (3.18)$$

where v_{ij}^r and v_{ij}^φ are the radial and azimuthal velocities in cell $[i, j]$ and Δr_{ij} and $r_{ij} \Delta \varphi_{ij}$ are the size of the cell. This limitation on the time-step is called *Courant–Friedrichs–Lewy Condition* (CFL).

At the inner boundary of the grid, usually the cells are very narrow as we use a logarithmic grid, meaning Δr is very small and velocity v_φ is rather large, as $v_\varphi \approx \Omega_K \cdot r = \sqrt{\frac{GM}{r^3}} r = \sqrt{\frac{GM}{r}}$. So the the cells at the inner boundary will determine the CFL-Condition.

Usually each time-step is divided in several sub-steps (see section 3.2 and [Stone and Norman \(1992, ZEUS-2D\)](#)) for each quantity ξ (e.g. surface density, velocities, energy, ...):

1. The sourceterms of the equations 2.6, 2.13 and 2.15 are applied. The sourceterms are the terms on the right-hand side where no advection occurs.
2. Transport in radial direction processing the derivatives with respect to r .
3. Transport in azimuthal direction processing the derivatives with respect to φ .

The transport steps are usually alternated after each time-step (when not using the FARGO-Algorithm). So, each time-step can be illustrated as:

$$\xi \xrightarrow{\text{source terms}} \xi^a \xrightarrow{\text{radial transport}} \xi^b \xrightarrow{\text{azimuthal transport}} \xi^+$$

The idea of the FARGO-Algorithm ([Masset, 2000](#)) is now, to split up the azimuthal transport step into two sub-steps:

- 3a. A residual velocity transport step with $v_{ij}^{\varphi \text{res}} = v_{ij}^\varphi - \bar{v}_{ij}^\varphi$. This is the same as the original azimuthal transport but with a replaced velocity and has to be done for each cell individually.
- 3b. The advection by \bar{v}_{ij}^φ is done in two steps. Therefore \bar{v}_{ij}^φ is decomposed as the nearest integer and a remainder which by construction is lower or equal to 0.5. In the first step the material is shifted by the remainder, which can be achieved by the same as the original azimuthal transport since the remainder is lower or equal to 0.5. The second step just corresponds to an integer number of cells shift which is done by simple shifting all cells.

As $v_{ij}^{\varphi \text{res}} < \bar{v}_{ij}^\varphi$ the material in the cell $[i, j]$ is now relatively slower and therefore the time-step can be increased. But as the rings now move at different mean velocities it has to be guaranteed that the rings don't disconnect in one time-step due to shear. So the CFL-Condition changes to

$$\Delta t_{ij} < C \cdot \min \left\{ \frac{\Delta r_{ij}}{v_{ij}^r}, \frac{r_{ij} \Delta \varphi_{ij}}{v_{ij}^{\varphi \text{res}}}, \frac{1}{2} \left(\frac{v_{ij}^\varphi}{r_{ij} \Delta \varphi_{ij}} - \frac{v_{i+1j}^\varphi}{r_{i+1j} \Delta \varphi_{i+1}} \right)^{-1}, \dots \right\} \quad (3.19)$$

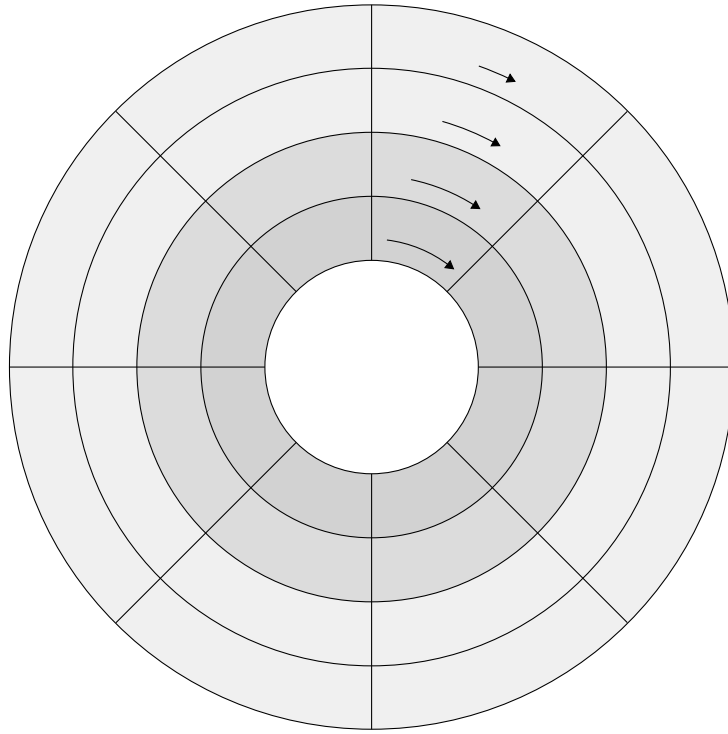


Figure 3.2: Illustrating the FARGO-Algorithm: The different rings (colored in different gray) rotate at different mean velocities, but all cells in one ring have the same mean velocity but different residual velocities. The disk rotates differentially and therefore the inner rings rotate at higher velocities than the outer rings.

where the second term accounts for the new residual velocity and the third term is a new term to guarantee that shear doesn't disconnect two neighboring cells $[i, j]$ and $[i + 1, j]$.

Figure 3.2 illustrates the idea of the FARGO-Algorithm where the rings rotate at different mean velocities.

3.5 Boundary conditions

As **FARGO** solves the Navier-Stokes equations which are partial differential equations boundary conditions must be given for the boundary of the region where the equations are solved. Usually Dirichlet boundary conditions are used for numerical calculations, which means that the values (and not the derivatives) of the quantities are given for the boundary.

In numerics boundary conditions can be implemented efficiently through the use of ghost cells. Ghost cells are one or more cells at the inner and outer boundary which are not set by the calculation routines, but are used by the routines to calculate values in the active cells. There is at least one ghost cell at the inner and outer boundary, but if higher-order derivatives are used, there have to be more of them. Figure 3.1 displays the radial ghost cells in gray color where as the azimuthal ghost cells are not needed, because in azimuthal direction a periodical boundary condition is used.

The ghost cells are set by the boundary conditions after each time-step. There are different

approaches how to set them. We used mainly open and reflecting boundary conditions, so this will be discussed in detail here. All boundaries are presented at the inner boundary. They need to be mirrored on the outer boundary.

3.5.1 Open boundary

Open boundary conditions allow material and energy to flow out of the computation domain and leave the system, thus the name open. Therefore the surface density and energy cells are just copied into ghost cells where as the velocity has to be checked if it points outwards which is allowed or points inwards. If it points inward it has to be set to zero, as there is no information known about the material outside which could flow in. So, the open boundary conditions are implemented as

$$\Sigma_{0j} = \Sigma_{1j} \quad (3.20)$$

$$\epsilon_{0j} = \epsilon_{1j} \quad (3.21)$$

$$v_{0j}^r = v_{1j}^r = \begin{cases} 0 & v_{2j}^r > 0 \\ v_{2j}^r & \text{otherwise} \end{cases} \quad (3.22)$$

Outflow boundary conditions are very natural boundary conditions as little reflections can occur. The problem is, that mass and energy can be lost through them but not come back.

The original version of **FARGO** used a different implementation of the open boundary:

$$v_{1j}^r = \begin{cases} 0 & v_{2j}^r > 0 \text{ or } \Sigma_{1j} < \bar{\Sigma}_0 \\ v_{2j}^r & \text{otherwise} \end{cases} \quad (3.23)$$

where $\bar{\Sigma}_i = \frac{1}{N} \sum_{j=0}^N \Sigma_{ij}|_{t=0}$ is the azimuthally averaged surface density at the beginning of the simulation.

3.5.2 Reflecting boundary

Reflecting boundary conditions are used to solve the problem of losing mass or energy through the boundaries. They are also named closed boundary conditions for this reason. Reflecting boundaries as the name suggests just reflect all energy and mass back. Their implementation is very simple

$$\Sigma_{0j} = \Sigma_{1j} \quad (3.24)$$

$$\epsilon_{0j} = \epsilon_{1j} \quad (3.25)$$

$$v_{0j}^r = v_{2j}^r \quad (3.26)$$

$$v_{1j}^r = 0 \quad (3.27)$$

The problem with reflecting boundaries is the reflection. Mass or energy can be collected at the boundaries and waves propagating through the whole disk can occur. Also oscillation of mass or energy at such boundaries are quite frequent.

3.5.3 Damping

To prevent these unwanted effects at the boundaries the disk can be damped towards there initial values at the boundaries. Usually this is done for the radial and angular velocity. The radial velocity is usually zero at the beginning (or same non-zero value to prevent gravitational collapse) whereas the azimuthal velocity is Keplerian.

The quantities are usually damped over a timescale τ which is measured in scales of $\frac{2\pi}{\Omega_K(r_{\min})}$ in a given damping range $(r_{\min}, r_{\min} \cdot d)$ where typical values for d range from 1.0 to 1.1, meaning that damping occurs within $\frac{\Delta r}{r} = 10\%$ at the inner region. Each quantity ξ is damped by

$$\xi(r) = (\xi(r) - \xi_0(r)) \cdot \exp \left[-dt \frac{\left(\frac{r - r_{\min}}{r_{\min} - r_{\min} \cdot d} \right)^2}{\tau \frac{2\pi}{\Omega_K(r_{\min})}} \right] + \xi_0(r) \quad (3.28)$$

Damping is not a boundary condition and so it is not updating the ghost cells. Therefore another routine must handle this.

3.6 Self gravity

To include self-gravity, the gravitational potential as described in section 2.3 has to be added to the Navier-Stokes equations as an external force. As we use a two-dimensional disk, we have to modify the equation 2.21 to

$$\Psi(\vec{r}) = -\mathcal{G} \iint \frac{\Sigma(\vec{r}')}{[(\vec{r} - \vec{r}')^2 + \epsilon^2]^{\frac{1}{2}}} d\vec{r}' \quad (3.29)$$

where Σ denotes surface density field and ϵ softening length. The softening length ϵ has two reasons: On the one hand it avoids singularity when $\vec{r} = \vec{r}'$ and on the other hand takes account for the infinitesimal height of the disk. The typical value used in our simulations was $\epsilon = 0.01$.

To reduce the computational time needed to calculate the potential it is rewritten as a convolution product to calculate it in Fourier space. With $M = \Sigma(\vec{r})$ and $K = (\vec{r}^2 + \epsilon^2)^{-\frac{1}{2}}$ it can be written as

$$\Psi = -\mathcal{G} [M * K] = -\mathcal{G} \mathcal{F}^{-1} [\mathcal{F}(M) \cdot \mathcal{F}(K)] \quad (3.30)$$

As $\mathcal{F}K$ is the same for all time-steps and the Fourier transformation can be calculated with Fast Fourier Transforms (FFT) the number of operations used to calculate the potential can be reduced from $\mathcal{O}(N^2)$ to $\mathcal{O}(N \ln N)$.

A problem using (periodic) discrete Fast Fourier Transforms is the periodicity. For example if we assume a singular mass density in one dimension where $M = 1$ for $x = 0.1$ and $M = 0$ for all other values of x and a periodic kernel with $\epsilon = 0.01$ in one dimension we can calculate the

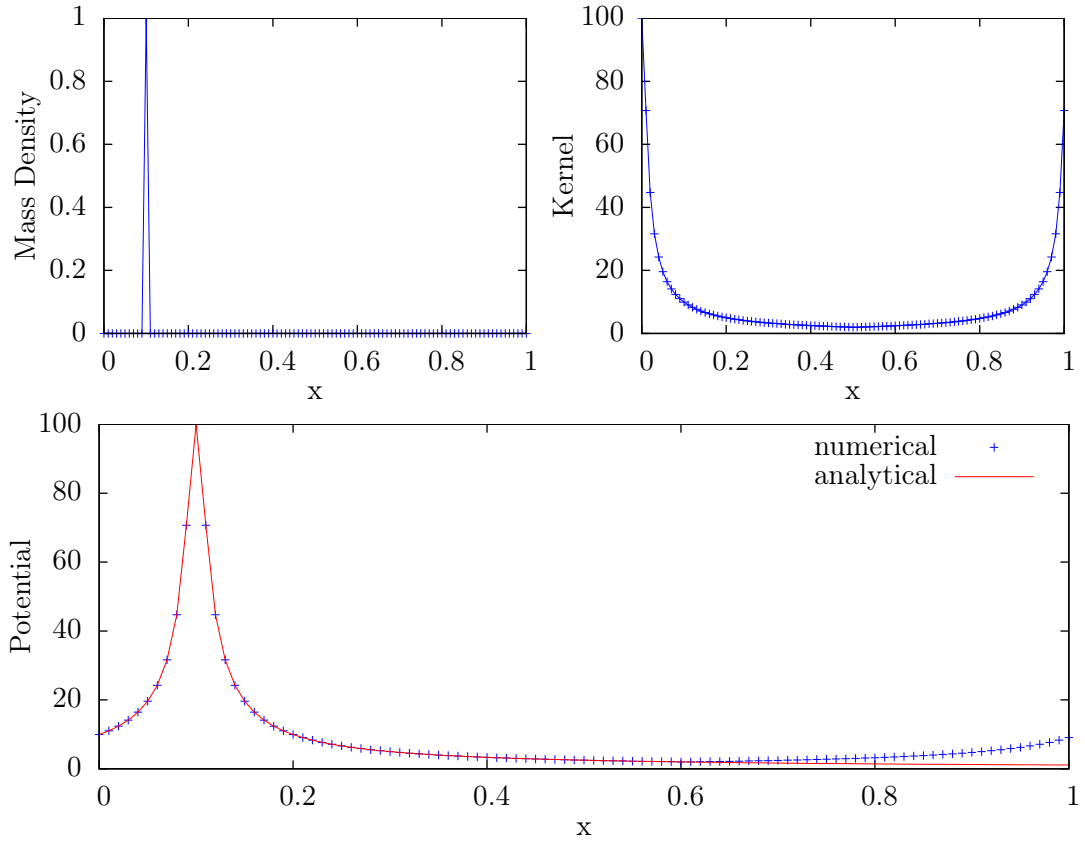


Figure 3.3: One-dimensional illustration of the alias issue. In the upper left panel is the surface density with a single singular mass density at $r = 0.1$. The upper right panel displays the periodic kernel. The lower panel shows the numerical potential obtained by FFT (blue crosses) and the analytical calculated potential (red curve).

analytical potential:

$$M(x) = \delta(x - 0.1) \quad (3.31)$$

$$K(x) = \frac{1}{\sqrt{x^2 + 0.01^2}} \quad (3.32)$$

$$\Psi(x) = -\mathcal{G} \int \frac{\delta(x' - 0.1)}{\sqrt{(x - x')^2 + 0.01^2}} dx' = -\mathcal{G} \frac{1}{\sqrt{(x - 0.1)^2 + 0.01^2}} \quad (3.33)$$

Figure 3.3 displays the calculated analytical potential and the potential calculated by discrete FFT. The analytical potential is not periodic as expected, however the numerical potential is always periodic (because of the periodic kernel) and its value differ from the analytical one for $r > 0.5$.

This problem is called aliasing and can be solved by doubling the space in radial direction and filling the additional news cells with zero mass. In azimuthal direction this problem does not occur as the potential is here periodic.

Another issue is, that **FARGO** uses polar coordinates, and equation 3.29 reads as

$$\Psi(r, \varphi) = -\mathcal{G} \int_{r_{\min}}^{r_{\max}} \int_0^{2\pi} \frac{\Sigma(r', \varphi')}{\sqrt{r^2 + r'^2 + 2rr' \cos(\varphi - \varphi') + \epsilon^2}} r' dr' d\varphi' \quad (3.34)$$

where r_{\min} and r_{\max} are respectively the radii of the inner and outer edge of the disk. This equation can be written as a convolution product with the variables $\{u = \ln \frac{r}{r_{\min}}, \varphi\}$ (Binney and Tremaine, 1987) and if ϵ scales with r . Then equation 3.34 can be written as

$$\Psi(u, \varphi) = -\mathcal{G} r_{\min} e^{-\frac{u}{2}} \int_0^{u_{\max}} \int_0^{2\pi} S(u', \varphi') K(u - u', \varphi - \varphi') du' d\varphi' \quad (3.35)$$

where S and K are defined as

$$S(u, \varphi) = \Sigma(u, \varphi) e^{\frac{3u}{2}} \quad (3.36)$$

$$K(u, \varphi) = \left[\left(1 + \left(\frac{\epsilon}{r_{\min} e^u} \right)^2 \right) e^u + e^{-u} - 2 \cos \varphi \right]^{-\frac{1}{2}} \quad (3.37)$$

But as Baruteau (2008) points out, there is a problem with radial self-acceleration when for example using a singular distribution for Σ . If we assume $\Sigma = \delta(u_d, \varphi_d)$ equation 3.35 yields:

$$\Psi(u, \varphi) = -\mathcal{G} r_{\min} e^{-\frac{u}{2}} S(u_d, \varphi_d) K(0, 0) = -\frac{\mathcal{G} (r_{\min})^2 e^{-\frac{3u_d+u}{2}}}{\epsilon} \quad (3.38)$$

which is proportional to $e^{-\frac{u}{2}}$ if ϵ scales with r as assumed.

Baruteau suggests to solve the problem by calculating directly the self-gravitating accelerations g_r and g_φ . Akin to the potential, these accelerations read as convolution products. The radial self-gravitating acceleration can be written as

$$g_r(u, \varphi) = -\mathcal{G} e^{-\frac{u}{2}} \int_0^{u_{\max}} \int_0^{2\pi} S_r(u', \varphi') K_r(u - u', \varphi - \varphi') du' d\varphi' + \mathcal{G} r_{\min} e^u \Sigma(u, \varphi) \frac{\Delta u \Delta \varphi}{\epsilon} \quad (3.39)$$

where Δu and $\Delta \varphi$ are the mesh sizes and S_r and K_r are given by

$$S_r(u, \varphi) = \Sigma(u, \varphi) e^{\frac{u}{2}} \quad (3.40)$$

$$K_r(u, \varphi) = \frac{1 + \left(\frac{\epsilon}{r_{\min} e^u} \right)^2 - e^{-u} \cos \varphi}{\left[2(\cosh u - \cos \varphi) + \frac{\epsilon^2}{(r_{\min})^2 e^u} \right]^{\frac{3}{2}}} \quad (3.41)$$

As $K_r(0, 0) = \frac{r_{\min} e^u}{\epsilon}$ there is a corrective term in 3.39 to remove radial self-forces.

The azimuthal self-gravitating acceleration can be written as

$$g_\varphi(u, \varphi) = -\mathcal{G} e^{-\frac{3u}{2}} \int_0^{u_{\max}} \int_0^{2\pi} S_\varphi(u', \varphi') K_\varphi(u - u', \varphi - \varphi') du' d\varphi' \quad (3.42)$$

with S_φ and K_φ given by

$$S_\varphi(u, \varphi) = \Sigma(u, \varphi) e^{-\frac{3u}{2}} \quad (3.43)$$

$$K_\varphi(u, \varphi) = \frac{\sin \varphi}{\left[2(\cosh u - \cos \varphi) + \frac{\epsilon^2}{(r_{\min})^2 e^u} \right]^{\frac{3}{2}}} \quad (3.44)$$

As $K_\varphi(0, 0) = 0$ no corrective term in equation 3.42 is needed.

The accelerations g_r and g_φ are now used by FARGO to update v_r and v_φ in each time-step. Therefore only S_r and S_φ have to be calculated each time-step by FFT. K_r and K_φ only have to be calculated once as they do not change over time.

More details on the implementation of self-gravity can be found in Baruteau (2008, Chapter 3.2).

3.7 Energy equation

The original FARGO code only implements an isothermal equation of state and therefore doesn't solve the energy equation (Equation 2.15). Baruteau (2008) added a third sub-step and introduced a basic energy equation:

$$\frac{\partial e}{\partial t} + \nabla \cdot (e \vec{v}) = -p \nabla \cdot \vec{v} + Q_+ - Q_- \quad (3.45)$$

where $e = \epsilon \Sigma$ is the thermal energy density (thermal energy per unit area) and p is the vertically integrated pressure. The first term on the right-hand side includes compressive heating where as Q_+ and Q_- are for other heating and cooling source terms.

The Q_+ heating term is implemented as viscous heating (see equation 2.49) and can be switched off or decreased by a constant factor on demand. There is also an additional heating term arising from the heat flux from the artificial viscosity, required to smooth shocks with a staggered-mesh code (Stone and Norman, 1992):

$$Q_+^{\text{art}} = -q_r \frac{\partial v_r}{\partial r} - q_\varphi \frac{\partial v_\varphi}{\partial \varphi} \quad (3.46)$$

where q_r and q_φ are given by equations 3.12 and 3.13.

The Q_- cooling term is implemented as local radiative cooling (described in section 3.8) or a simple β -cooling law (see equation 2.45). They can be switched on and off independently. The β -cooling has to be handled with care in combination with a α -viscosity model, as it is unstable (see equation 2.55).

3.8 Local radiative cooling

The cooling term Q_- corresponds to the $\nabla \vec{F}$ term in equation 2.15. We assume now, that the amount of energy transported by radiation in the vertical direction (z -axis) is much larger than that transported horizontally ((r, φ) -plane). This assumption is valid, if the vertical

extent of the disk remains small compared to extent in the horizontal direction. If we now integrated $\nabla \vec{F}$ over the disk height we get

$$Q_- = \int_{-\infty}^{\infty} \nabla \vec{F} dz \approx \int_{-\infty}^{\infty} \frac{\partial F_z}{\partial z} dz = F_z(H) - F_z(-H) = 2F_z(H) \quad (3.47)$$

\vec{F} is the frequency-integrated radiation flux it reads as

$$\vec{F} = -\frac{16\sigma_R}{3\kappa\rho} T^3 \nabla T \quad (3.48)$$

where σ_R is the Stefan-Boltzmann constant, κ the frequency-integrated opacity coefficient and ρ the mass density. We can now rewrite Q_- (Kley and Crida, 2008; Kley *et al.*, 2005; D'Angelo *et al.*, 2003) as

$$Q_- = 2[F_z(H) - F_z(0)] \approx -\frac{16\sigma_R}{3\kappa\rho} \left[\frac{T^4(H)}{H} - \frac{T^4(0)}{H} \right] \quad (3.49)$$

and with $\tau = \kappa\rho H = \frac{1}{2}\kappa\Sigma$ for inner parts of the a circumstellar disk where $T^4(0) \gg T^4(H)$ this yields:

$$Q_- = \frac{2\sigma_R T^4}{\frac{3}{4}\tau} \quad (3.50)$$

where T is the disk mid-plane temperature.

Equation 3.50 represents a fairly good approximation when the medium is very optically thick ($\tau \gg 1$), but this is not true for all parts of our simulated disks (especially between spiral arms the density can be very low). Hubeny (1990) found an appropriate relationship, which represents a generalization of the gray model of classical stellar atmospheres in local thermodynamic equilibrium. Therefore we use the following expression for Q_- :

$$Q_- = \frac{2\sigma_R}{\tau_{\text{eff}}} T^4 \quad (3.51)$$

where τ_{eff} is given by Hubeny's theory:

$$\tau_{\text{eff}} = \frac{3}{8}\tau + \frac{\sqrt{3}}{4} + \frac{1}{4\tau} \quad (3.52)$$

For the Rosseland mean opacity κ we adopt power-law dependencies on temperature and density described by Lin and Papaloizou (1985), where

$$\kappa = \kappa_0 \rho^a T^b \quad (3.53)$$

for various opacity regimes. Each opacity regime is described by a minimum and maximum (density dependent) temperature and has a given κ_0 , a and b . Table 3.1 gives an overview of the constants for the different opacity regimes.

To avoid discontinuities we used a smoothed function which connects the different regimes. Figure 3.4 shows the Rosseland mean opacity for a fixed density value of $\rho = 1 \cdot 10^{-8} \text{ cm}^{-3} \text{ g}$. The horizontal lines mark the different regimes described in table 3.1. The red dotted lines are the power-laws for the specific regime whereas the blue curve is the smoothed function we used in the code.

Table 3.1: Details of the various opacity regimes by type, showing the transition temperature and the constants κ_0 , a , b . All values are quoted in cgs units. See [Lin and Papaloizou \(1985\)](#) for further details.

#	regime	κ_0 [cm ² g ⁻¹]	a	b	temperature range [K]	
					from	to
1	Ice grains	$2 \cdot 10^{-4}$	0	2	0	170
2	Sublimation of ice grains	$2 \cdot 10^{16}$	0	-7	170	210
3	Dust grains	$5 \cdot 10^{-3}$	0	1	210	$4.6 \cdot 10^3 \rho^{\frac{1}{15}}$
4	Sublimation of dust grains	$2 \cdot 10^{34}$	$\frac{2}{3}$	-9	$4.6 \cdot 10^3 \rho^{\frac{1}{15}}$	3000
5	Molecules	$2 \cdot 10^{-8}$	$\frac{2}{3}$	3	3000	$1.1 \cdot 10^4 \rho^{\frac{1}{21}}$
6	Hydrogen scattering	$1 \cdot 10^{-36}$	$\frac{1}{3}$	10	$1.1 \cdot 10^4 \rho^{\frac{1}{21}}$	$3 \cdot 10^4 \rho^{\frac{4}{75}}$
7	bound-free & free-free	$1.5 \cdot 10^{20}$	1	$-\frac{5}{2}$	$3 \cdot 10^4 \rho^{\frac{4}{75}}$	—

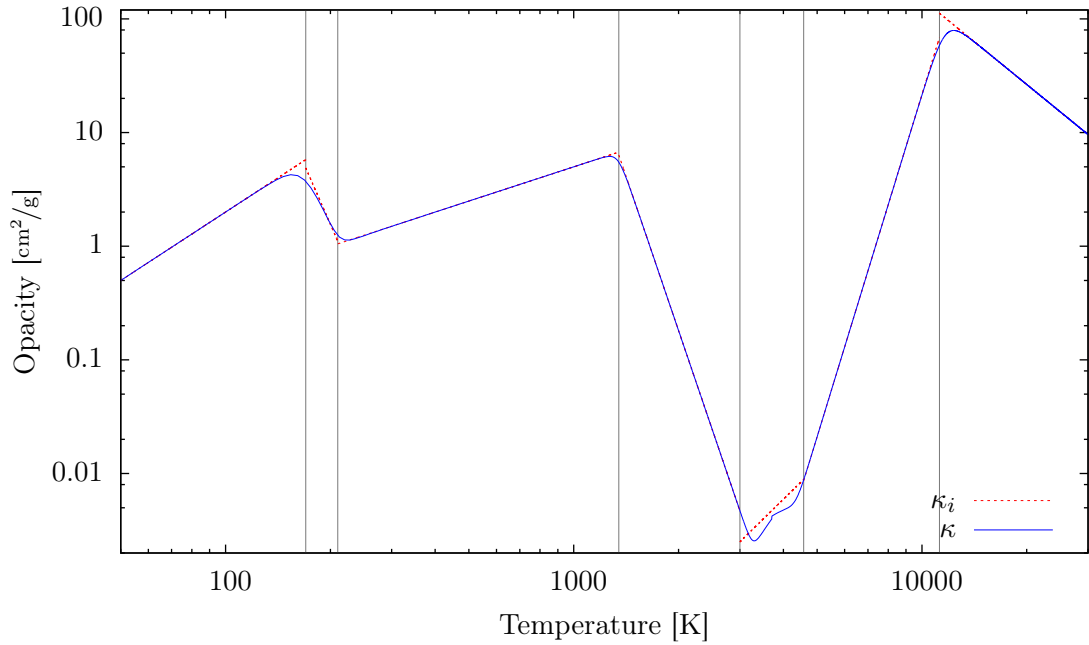


Figure 3.4: Opacity $\kappa(T)$ at density $\rho = 1 \cdot 10^{-8}$ g/cm³. The vertical lines separate the different regimes described in table 3.1. The dotted red curve show the power-laws for each region whereas the blue curve is the smoothed function used in the code.

3.9 Tests

To test the implementation of the viscous heating and local radiative cooling, comparison calculations to the paper by [Kley and Crida \(2008\)](#) have been done.

[Kley and Crida](#) used a model with a central star mass M_{star} of one solar mass (M_{\odot}) and a total disk mass of $M_{\text{disk}} = 0.01 M_{\odot}$ within radii between $r_{\text{min}} = 0.4 r_{\text{jup}}$ and $r_{\text{max}} = 2.5 r_{\text{jup}}$. The model was initialized with a surface density profile of $\Sigma \propto r^{-\frac{1}{2}}$ and a temperature profile of $T \propto T^{-1}$. The velocities were pure Keplerian ($v_r = 0$, $v_{\varphi} = \sqrt{\frac{GM_{\text{star}}}{r}}$).

The viscosity in this model was of a constant value of $\nu = 10^{15} \text{ cm}^2/\text{s}$, which relates to an equivalent α of 0.004 at r_{jup} for a disc aspect ratio of $h = \frac{H}{r} = 0.05$.

The model is relaxed to its equilibrium by solving the full Navier-Stokes equations but without self-gravity. The evolution after 150 orbits is displayed in figure [3.5](#).

[Kley and Crida](#) used closed boundary conditions for the surface density and the temperature where as velocities were damped towards their initial values on a timescale of approximately the local orbital period. We used reflecting boundary conditions and did calculations with and without damping of velocities.

The surface density plots match very well for radii up to $2 r_{\text{jup}}$. The values beyond differ, because the surface density oscillates there around the equilibrium value and thus the density depends on which exact time is plotted.

The temperature plots have the same shape, but the values of [Kley and Crida](#) are a little bit higher especially for larger radii. The reason is that [Kley and Crida](#) included also the two-dimensional radiative flux in the (r, φ) -plane.

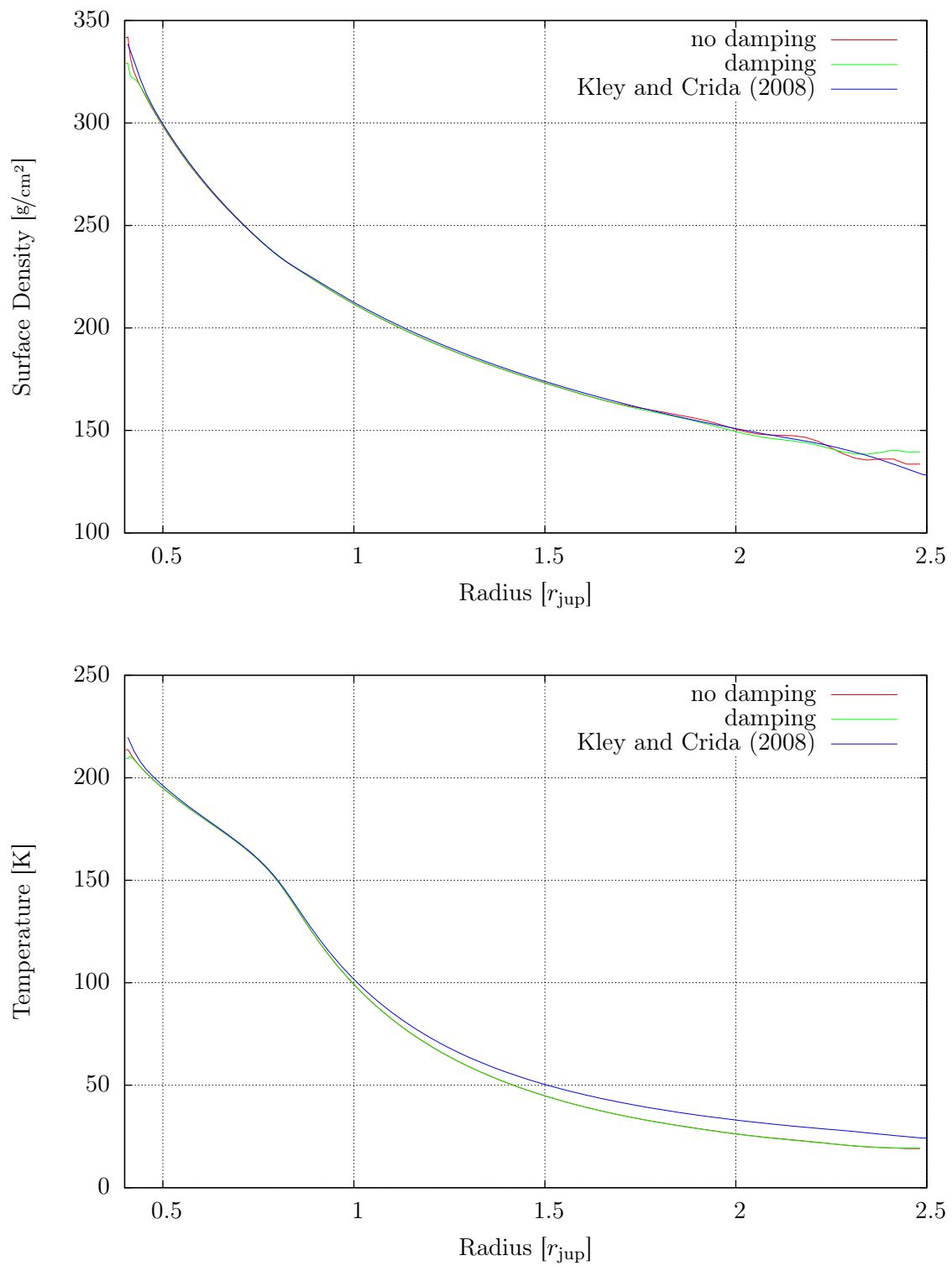


Figure 3.5: Comparison of surface density and temperature of the relaxed model with calculations done by [Kley and Crida \(2008\)](#)

4 Results

4.1 Isothermal disk

To show the possibility of fragmentation in more massive disks and to test the implementation of the self-gravity part in the code, the first calculations used a very simple, isothermal model with constant viscosity $\nu = 10^{15} \text{ cm}^2/\text{s}$.

We used a disk with a small radial extent ranging from 0.5 AU to 2.5 AU around a solar mass host star ($M_{\text{star}} = M_{\odot}$). The surface density Σ was initialized with a $\Sigma(r) = \Sigma_0 \cdot r^{-1.5}$ power-law with random variation of 10 % to remove axisymmetry (see figure 4.1, upper panel). The disk aspect ratio was set to $h = 0.05$ and no energy equation was solved. At initial state, the gas was rotating at

$$\Omega(r) = \left(\Omega_K(r)^2 [1 - (1 + \sigma - 2f)h^2] - \frac{g_r(r)}{r} \right)^{\frac{1}{2}} \quad (4.1)$$

which imposes a strict balance between gravitational force due to the central star, the pressure force and the centrifugal force corrected by the self-gravity acceleration given by equation 3.39. Here is $\sigma = 1.5$ the exponent of the $\Sigma(r)$ power law ($\Sigma(r) = \Sigma_0 \cdot r^{-\sigma}$) and f the flaring index defined by

$$h(r) = h(r_0) \left(\frac{r}{r_0} \right)^f \quad (4.2)$$

which describes the radial dependency of the disk's aspect ratio.

Figure 4.2 shows the $\Omega(r)$ at $t = 0$ in terms of $\Omega_K(r)$. The radial velocity is initialized with

$$v_r(r) = -\frac{3}{\Sigma r^{\frac{1}{2}}} \frac{\partial}{\partial r} \left[\nu \Sigma r^{\frac{1}{2}} \right] \quad (4.3)$$

which is evaluated from the combination of mass and angular momentum equations (Lynden-Bell and Pringle, 1974).

We did four calculations with disk masses of $M_{\text{disk}} = 0.05 M_{\text{star}}$, $M_{\text{disk}} = 0.1 M_{\text{star}}$, $M_{\text{disk}} = 0.2 M_{\text{star}}$ and $M_{\text{disk}} = 0.4 M_{\text{star}}$ to test the Toomre criterion (see section 2.3). The two lighter disks do not satisfy Toomre's criterion at all, whereas the $0.2 M_{\text{star}}$ mass disk satisfies it for radii larger than 1 AU. The $0.4 M_{\text{star}}$ satisfies the Toomre criterion for all radii and therefore should fragment.

We used the original **FARGO** open boundaries (see section 3.5) which does not allow that much mass to flow outwards as normal boundary conditions and a grid with 256 cells in radial and 128 cells in azimuthal direction. All disks were evolved for a time of 50 orbits at $r = 1$ AU which corresponds to a evolution over 50 years. The calculations were done using an 8-core 3.0 GHz Intel[®] Xeon[™] E5450 system.

Expectedly, we do not get fragmentation for the two disks which do not satisfy Toomre's stability criterion, whereas the two more massive disks do fragment. Table 4.1 summarizes the calculations. In figure 4.3 the surface density of the disks with masses $0.1 M_{\text{star}}$, $0.2 M_{\text{star}}$ and $0.4 M_{\text{star}}$ are plotted. The $0.05 M_{\text{star}}$ disk does not show any major changes after the simulation of 50 years.

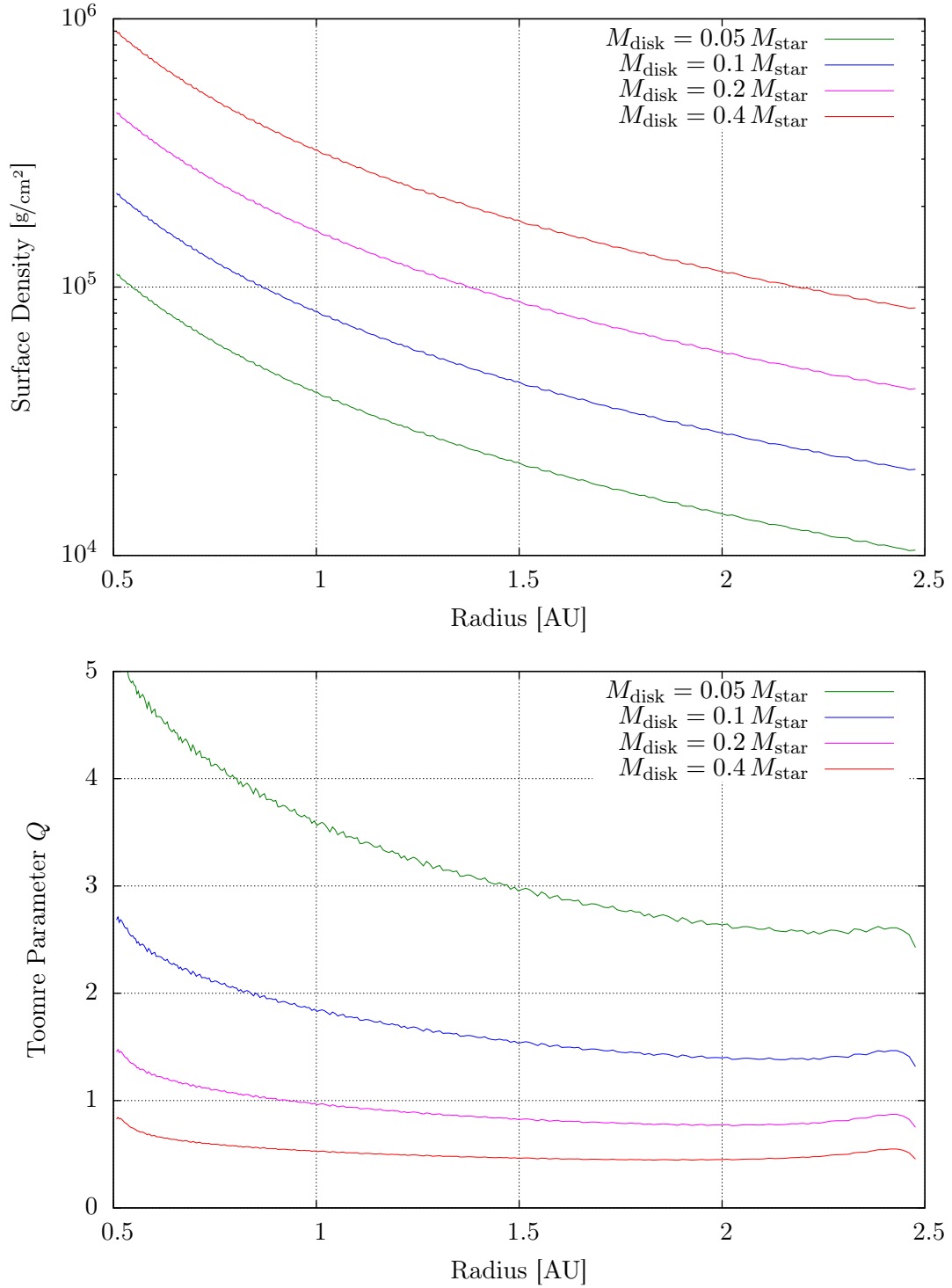


Figure 4.1: Surface density (upper panel) and Toomre parameter (lower panel) for the isothermal model at $t = 0$ with the original **FARGO** open boundary condition. The fluctuations are caused by the 10 % random initialization. The $0.2 M_{\text{star}}$ disk (purple curve) satisfies the Toomre criterion ($Q < 1$) for $r > 1$ AU whereas the $0.4 M_{\text{star}}$ disk (red curve) satisfies the Toomre for all radii.

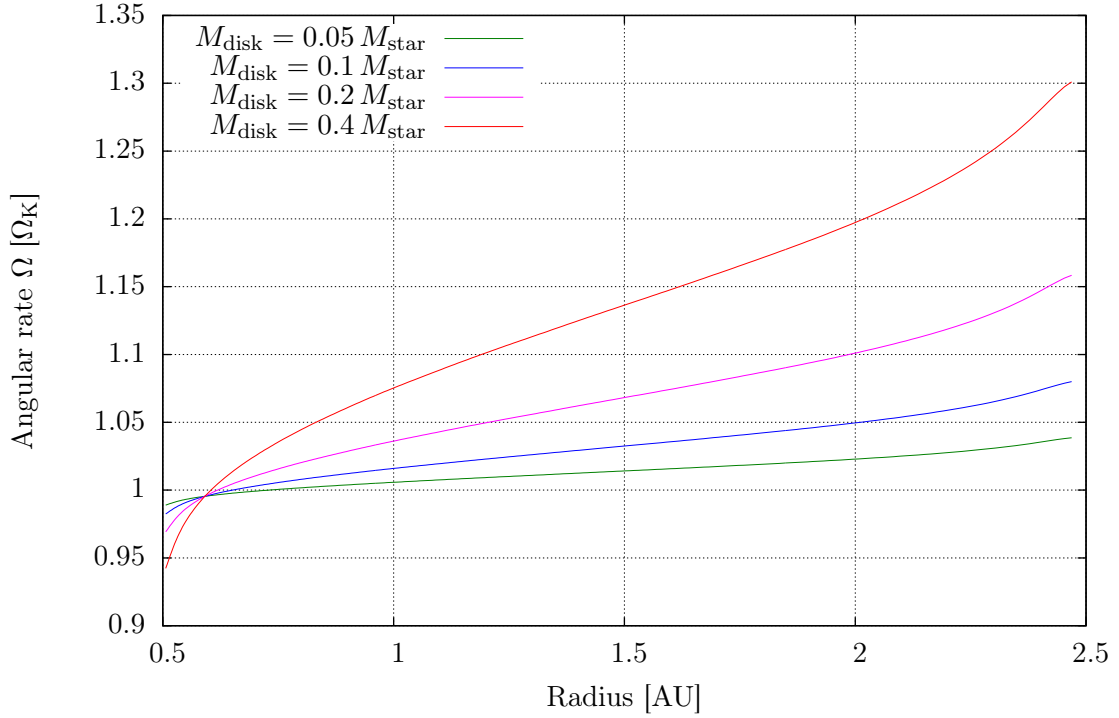


Figure 4.2: Angular rotation rate Ω in terms of Kepler rate Ω_K (see equation 2.2) at $t = 0$. The angular rate is self-gravity compensated and therefore not equal to Ω_K .

Figure 4.3 shows some artifacts especially on the outer boundary due to the implemented boundary conditions in **FARGO**. Therefore, we redid all calculations with normal open boundary conditions (see equation 3.23) with a resolution of 256 cells in radial and 384 cells in azimuthal direction. Figure 4.4 shows the disk with normal open boundary conditions. For the low mass disks there is no significant difference, but the $0.2 M_{\text{star}}$ disks does not fragment into clumps even after 500 years. The $0.4 M_{\text{star}}$ disk fragments into clumps after only a very short time, and all clumps beside of one will leave the computational domain within 50 years as the disk is now really open at the boundaries. This may also be the reason why the $0.2 M_{\text{star}}$ disk does not fragment as mass left the system too rapidly through the outer boundary. Figure 4.5 shows the evolution of the disk masses over time.

After 50 years the $0.4 M_{\text{star}}$ disk has nearly all its mass left in one density clump orbiting

Table 4.1: Fragmentation of a **isothermal disk** depending on its mass with the original **FARGO** open boundary condition. See section 4.1 and figure 4.3 for detailed information about the models.

	1	2	3	4
disk mass	$0.05 M_{\text{star}}$	$0.1 M_{\text{star}}$	$0.2 M_{\text{star}}$	$0.4 M_{\text{star}}$
Σ_0	40467.9 g/cm^2	80935.9 g/cm^2	161872 g/cm^2	323744 g/cm^2
satisfies Toomre criterion	no	no	$r > 1 \text{ AU}$	yes
fragmentation	no	no	yes	yes

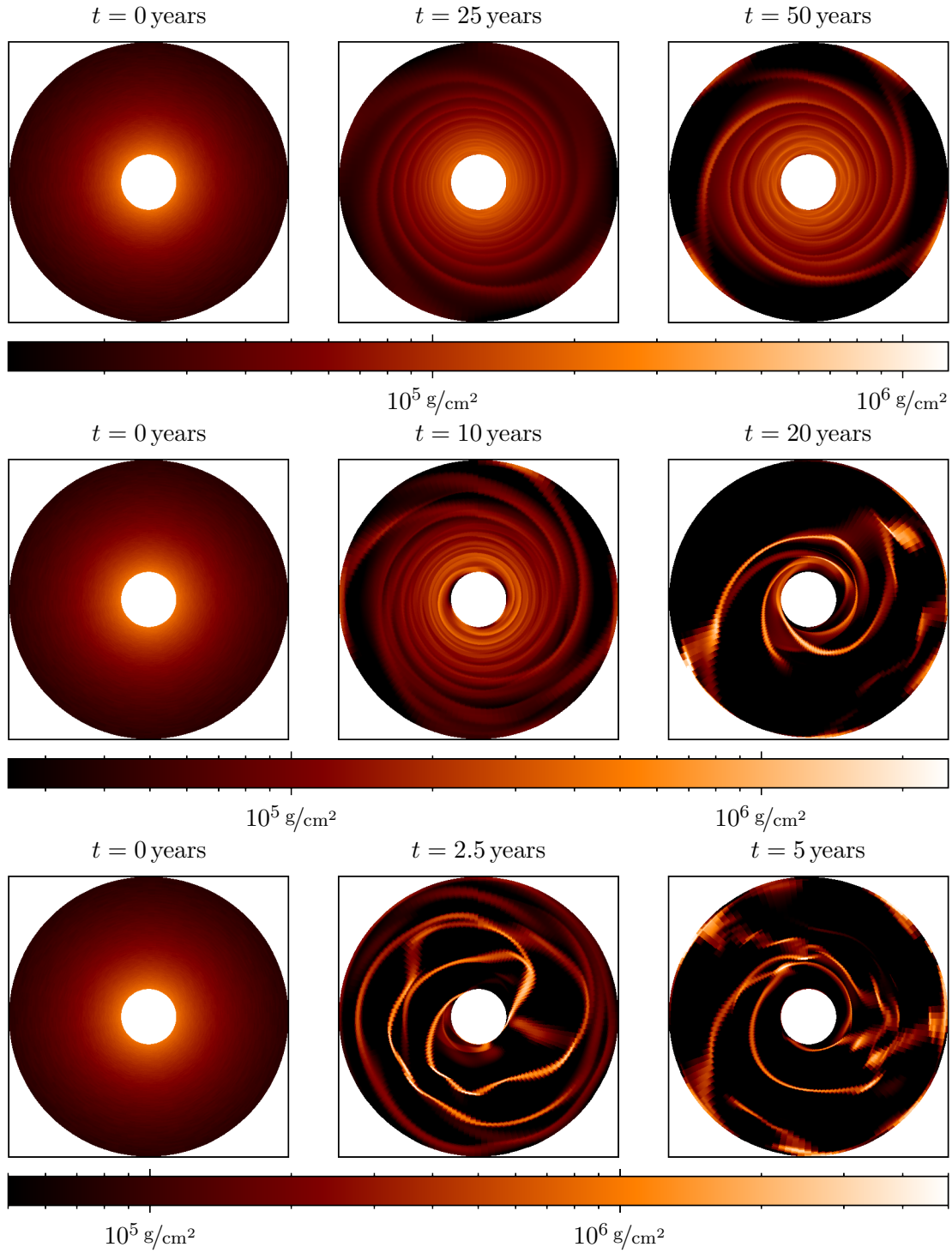


Figure 4.3: Time evolution of the disk's surface density with masses of $0.1 M_{\text{star}}$ (upper row), $0.2 M_{\text{star}}$ (middle row) and $0.4 M_{\text{star}}$ (lower row) with the **original FARGO open boundary condition**. The disks ranges from 0.5 AU to 2.5 AU. The $0.1 M_{\text{star}}$ mass disk doesn't fragment after the simulation of 50 years, whereas the $0.2 M_{\text{star}}$ disk fragments after about 20 years. The $0.4 M_{\text{star}}$ disk fragments after a very short time of only a few years. The color-axis of the different disks has been adjusted to have the same coloring at the start point.

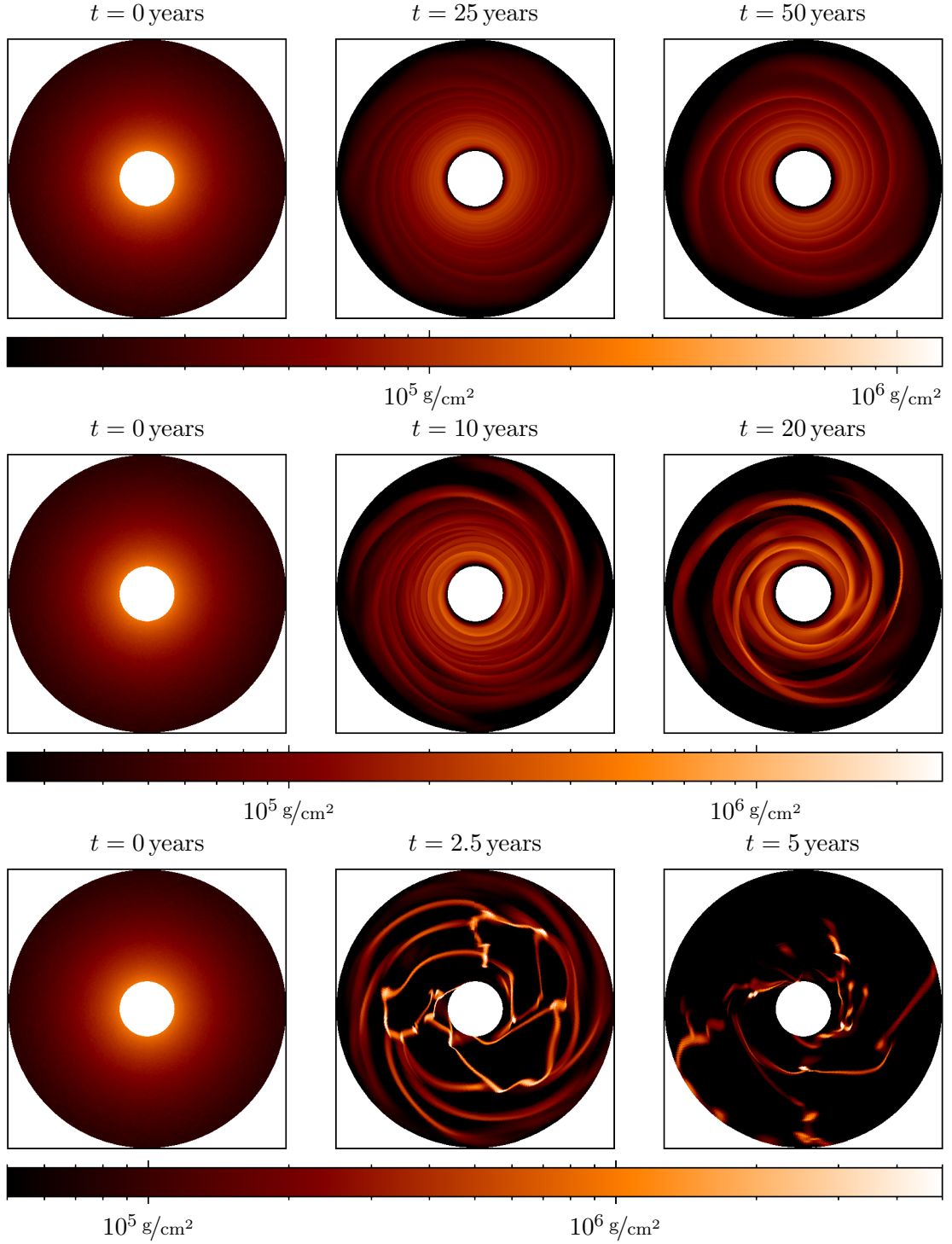


Figure 4.4: Time evolution of the disk's surface density with masses of $0.1 M_{\text{star}}$ (upper row), $0.2 M_{\text{star}}$ (middle row) and $0.4 M_{\text{star}}$ (lower row) with **open boundary condition**. The disks ranges from 0.5 AU to 2.5 AU. The $0.1 M_{\text{star}}$ mass disk doesn't fragment after the simulation of 50 years. The $0.2 M_{\text{star}}$ disk shows unregular spiral arms, but does not fragment into clumps even after 500 years. The $0.4 M_{\text{star}}$ disk fragments after a very short time of only a few years. The color-axis of the different disks has been adjusted to have the same coloring at the start point.

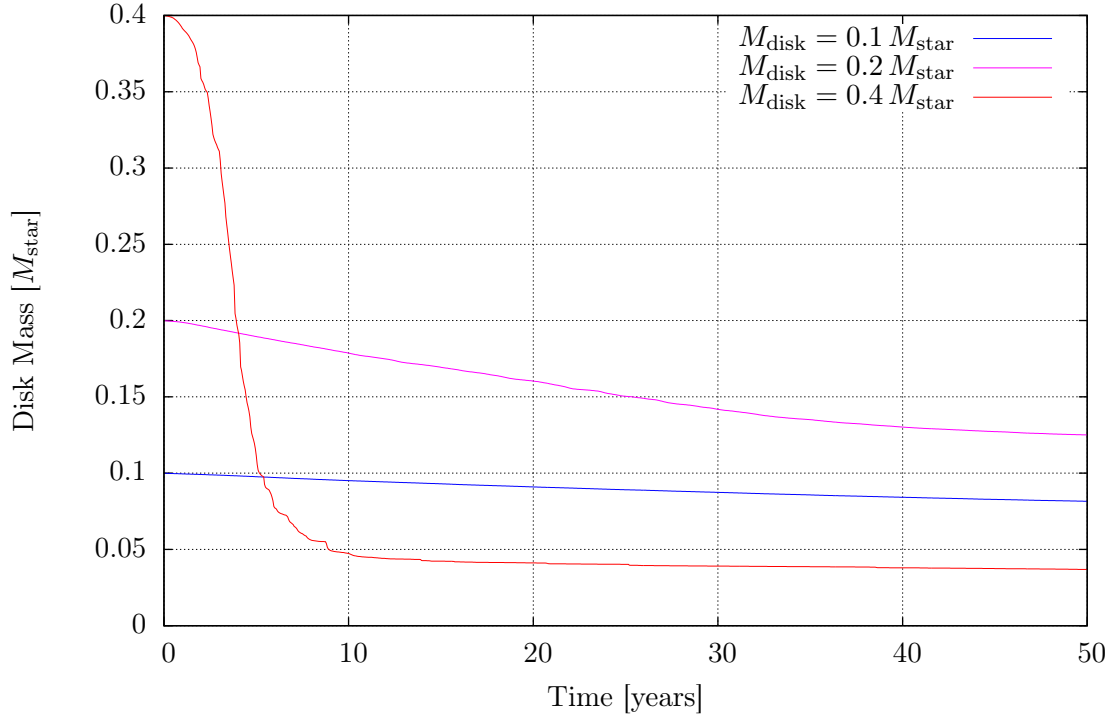


Figure 4.5: Evolution of disk mass over time. The higher the disk mass the more mass is lost over time. The $0.1 M_{\text{star}}$ disk loses only 18 % of mass in the first 50 years whereas the $0.2 M_{\text{star}}$ loses 37 % and the $0.4 M_{\text{star}}$ even 91 %.

around the star a roughly 1 AU.

As in the first two simulations the disk was very small with an radial extent only ranging from 0.5 AU to 2.5 AU, we did another simulation with a rather larger disk ranging from 10 AU to 100 AU and a disk mass of $M_{\text{disk}} = 0.5 M_{\text{star}}$. The disk satisfies Toomre’s criterion at all radii as $Q \approx 0.5$.

Within 1000 years the disk fragments into several clumps (see figure 4.6). Some of them collide and grow into bigger clumps. After about 4000 years only one clump at about 20 AU is left, which contains nearly all mass left ($\approx 0.04 M_{\text{star}} \approx 42 M_{\text{jup}}$). All other clumps have collided or left the computational domain. Figure 4.7 shows the evolution of the disk mass.

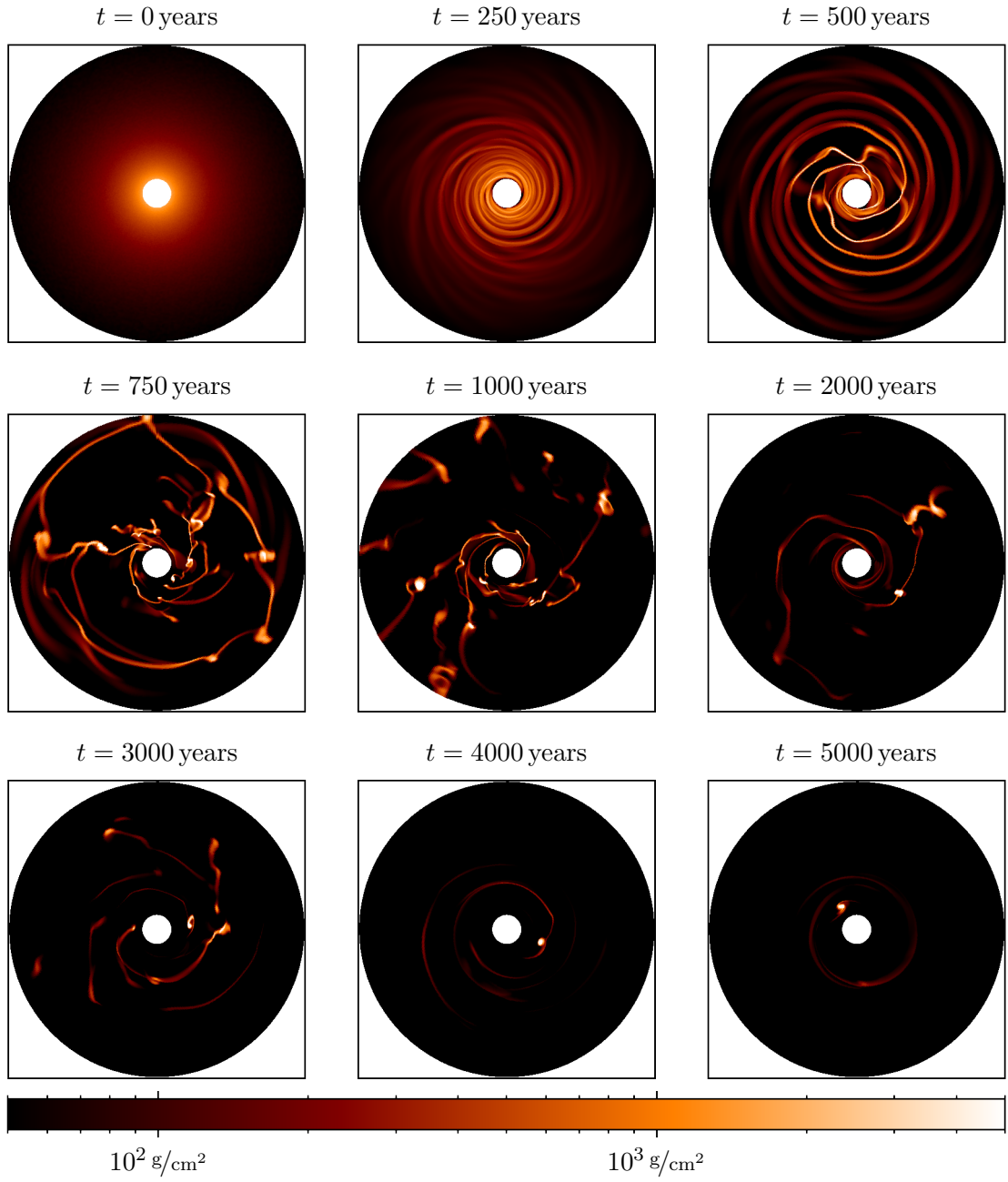


Figure 4.6: Time evolution of the disk's surface density with a mass of $0.5 M_{\text{star}}$ and a **large disk** with radial extent ranging from 10 AU to 100 AU. The fragmentation occurs within 1000 years.

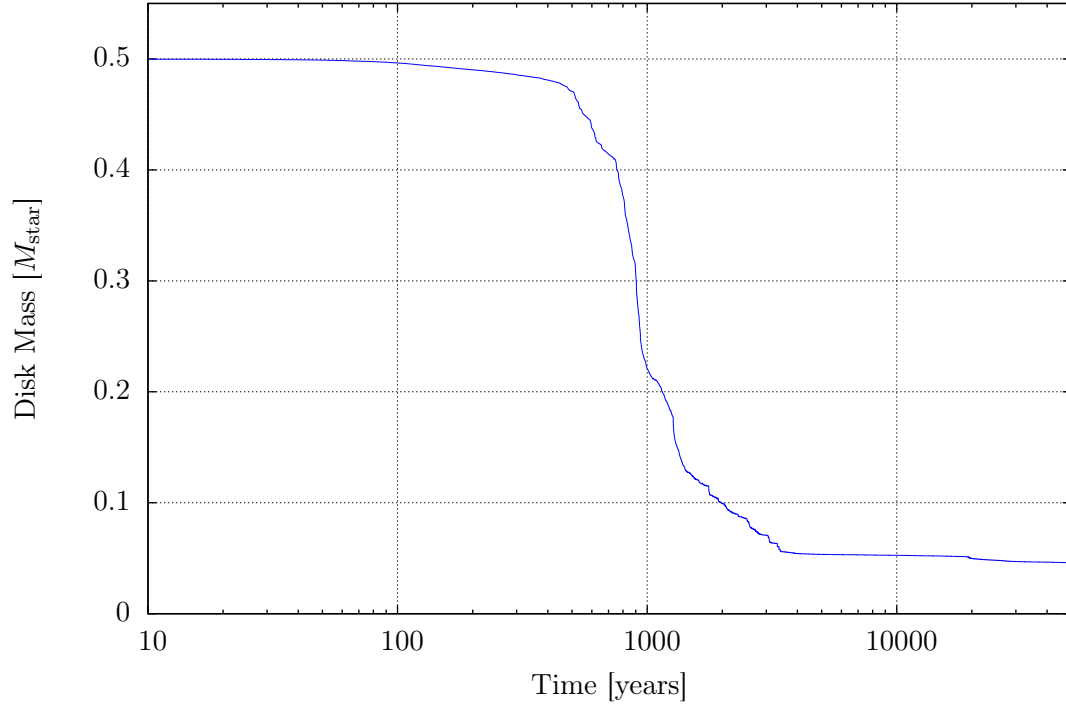


Figure 4.7: Evolution of disk mass over time of the $0.5 M_{\text{star}}$ mass disk. Nearly all mass lost is lost during the first 5000 years.

4.2 Disks with cooling

In section 2.4.1 we described an estimation for cooling and derived a correlation between the α -parameter of viscosity (Shakura and Sunyaev, 1973) and the local cooling rate β (see equation 2.55). In this section we examine the influence of the α -parameter on the fragmentation of the disk using local radiative cooling.

In all of these simulations we used a rather large disk ranging from $1 r_{\text{jup}} = 5.2 \text{ AU}$ to $10 r_{\text{jup}} = 52 \text{ AU}$ around a solar mass host star. The disk has a total mass of $0.1 M_{\text{star}}$ and an aspect ratio of $h = 0.05$. We ran the simulation for α values of 0.005, 0.01, 0.02, 0.04, 0.06, 0.08 and 0.5.

To have a well defined initial conditions, we bring all models in the first step into local thermal equilibrium. We initialized our simulations with a density profile of $\Sigma(r) = \Sigma_0 \cdot r^{-1}$ and a specific energy profile of $\epsilon(r) = \epsilon_0 \cdot r^{-1}$ and an energy equation with radiative local cooling using reflecting boundary conditions to keep the disk mass constant (see figure 4.8). For this purpose we perform quasi one-dimensional calculations using a grid with only 4 cells in azimuthal direction. We assume that the equilibrium is reached, when the energy e does not change any more (see figure 4.9).

The temperature of models with higher α are higher than the models with lower α in thermal equilibrium as expected, because the higher viscosity heats the disks more efficiently as all heating is done by viscous dissipation (see equation 2.49). Also the higher viscosity models display a flatter density profiles.

We then used the radial profile of the surface density Σ and energy profile e to initialize the actual simulations with self-gravity. The density profile is perturbed by 10 % to remove axisymmetry. The velocities were initialized to have a strict balance between gravitational force due to the central star, the pressure force and the centrifugal force corrected by the self-gravity acceleration (see equations 4.1 and 4.3, where $\sigma = 1$ and $f = 0$)

We evolved all simulations over a timescale of 500 orbits (at $r = 1 \text{ AU}$) which corresponds to 500 years. To rule out problems with Toomre's criterion we did the simulations for the $\alpha = 0.02$ model also with a double disk mass. Both disk masses satisfy Toomre's criterion for $r \gtrsim 4.5 \text{ AU}$ (see figure 4.10).

All simulations done with this setting do not show any fragmentation even after 1000 years. Figure 4.11 shows the disks with different α values after 500 years.

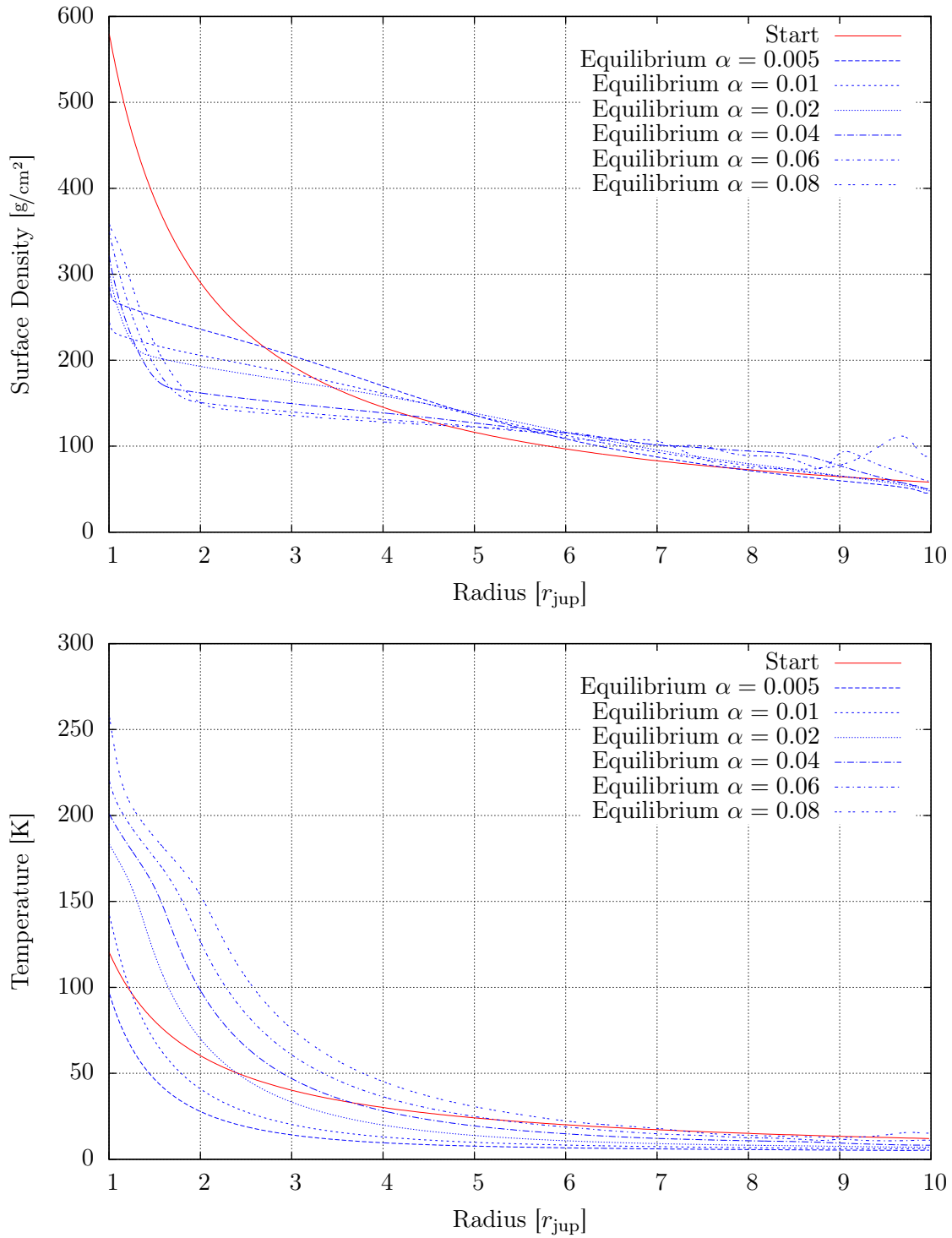


Figure 4.8: Surface density and temperature of the model at initialization (red curve) and at thermal equilibrium (blue curves) for different α values. The density fluctuations in the blue curves for radii larger than $\sim 7 r_{\text{jup}}$ are caused by oscillations around the equilibrium value.

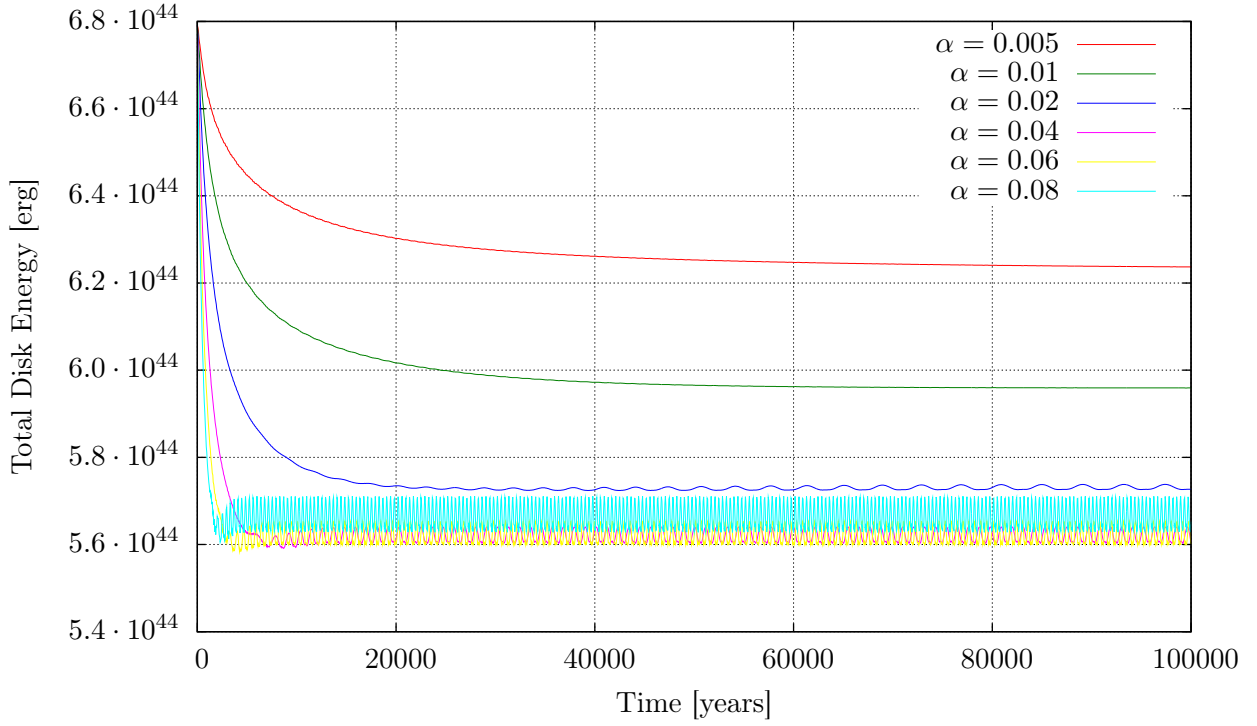


Figure 4.9: Evolution of total disk energy over time until equilibrium. The disks with small α values needed much longer to come to thermal equilibrium. Disks with large α are oscillating around a quasi equilibrium.

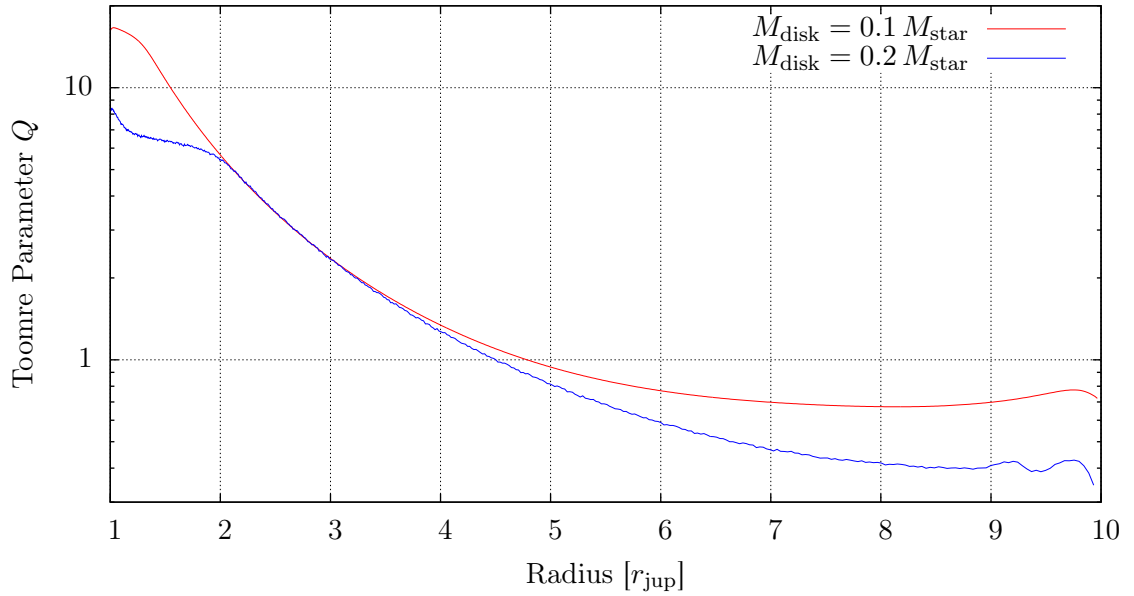


Figure 4.10: Toomre Parameter Q for $0.1 M_{\text{star}}$ and $0.2 M_{\text{star}}$ disk with $\alpha = 0.02$ in thermal equilibrium. Both satisfies Toomre's criterion for $r \gtrsim 4.5 \text{ AU}$.

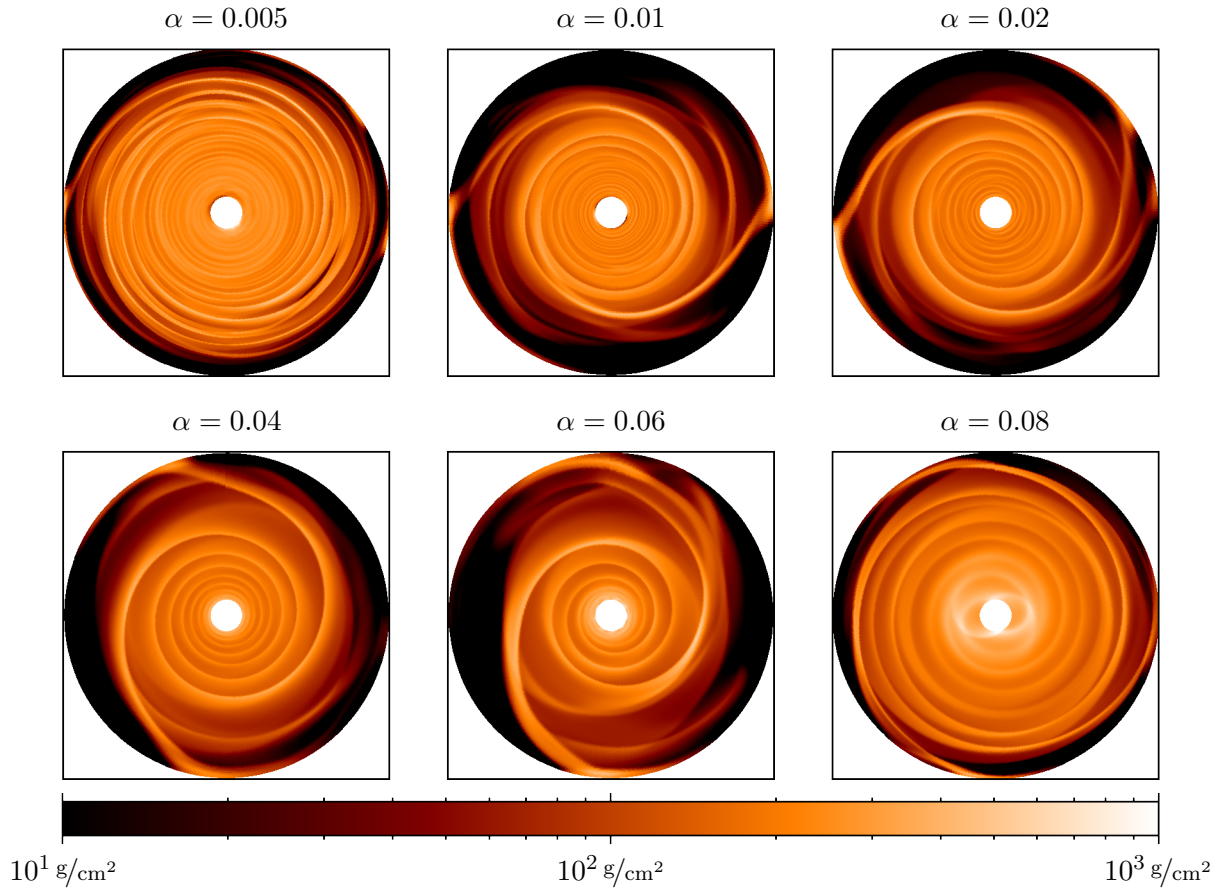


Figure 4.11: Time evolution of the disk's surface density after 500 years different values of α .

4.2.1 Comparison with SPH models

For this sequence of calculations, we adopted a disk model given by [Rice et al. \(2005\)](#). The radial extent of the disk ranges from 0.25 AU to 25 AU around a solar mass host star. The density profile is initialized with a $\Sigma(r) = \Sigma_0 \cdot r^{-1}$ power-law and the temperature is given by $T(r) = T_0 \cdot r^{-0.5}$. Like in all our models, the velocities were initialized to have a strict balance between gravitational force due to the central star, the pressure force and the centrifugal force corrected by the self-gravity acceleration (see equations 4.1 and 4.3, where $\sigma = 1$ and $f = 0.25$).

[Rice et al.](#) performed several simulations using a SPH (Smoothed Particle Hydrodynamics) code with heating by viscous dissipation and pdV work and cooling by a simple β -Cooling as introduced in equation 2.45. They used an $\alpha_{\text{SPH}} = 0.1$ for the viscous dissipation which corresponds to an $\alpha \approx 0.01$ ([Lodato and Rice, 2004](#), appendix) for our α -model by ([Shakura and Sunyaev, 1973](#)). They started their simulations for different masses with small β values that should fragment and then increased β simulation by simulation to check when it stops fragmenting. For the simulations comparable to ours, they get fragmentation for $\beta \lesssim 12$.

We consider disk masses of $M_{\text{disk}} = 0.25 M_{\text{star}}$ and $0.5 M_{\text{star}}$ ([Rice et al.](#) also considered a disk mass of $M_{\text{disk}} = 0.1 M_{\text{star}}$, but as we do not get fragmentation even for the more massive disks, we skipped this). Figure 4.12 shows the Toomre parameter for both disk masses. [Rice et al.](#) normalized the temperature, so that at the beginning of the simulation the disk has a minimum of $Q = 2$ at $r = 25$ AU, whereas our both disk have a $Q < 2$, so should be even more likely to fragment. We did all calculations with reflecting boundary conditions and some of them in addition with open boundary condition, but did not see any major changes on the question of fragmentation.

We used the α -model ([Shakura and Sunyaev, 1973](#)) for viscosity with $\alpha = 0.02$ and our local radiative cooling to cool our disk ($\gamma = \frac{7}{5}$). We do not see any fragmentation with our local radiative cooling. As described in section 2.4.1 the β -Cooling with viscous dissipation and α -viscosity is unstable and hence, we could not calculate direct analogues to compare with the results of [Rice et al.](#), but if we calculate the disk using β -Cooling and abstain from viscous heating the disk shows signs of fragmentation (see figure 4.13), but the Toomre parameter satisfies Toomre's criterion only for radii less than 4 AU (see figure 4.14).

As β -Cooling does not depend on any local factors the cooling rate is always the same, and the disks tend to have a lower temperature. To simulate this with our local radiative cooling, we calculated an additional sequence where we reduced our viscous dissipation by a factor λ of 10 and 100 in the calculations. The disk temperature decreases as expected (see figure 4.15), but no fragmentation occurred after 500 orbits which is shown in figure 4.16. Figure 4.17 shows the evolution of the Toomre parameter of the disk with different values of λ . The $0.25 M_{\text{star}}$ disk does not satisfy Toomre's criterion at any time, whereas the $0.5 M_{\text{star}}$ satisfies it at $t = 0$, but not in later time-steps. The increase of the Toomre parameter on the outer boundary is not caused by the FARGO open boundary conditions used in the simulations, as these effects also occur on calculations using the normal open boundary conditions.

We also tried to increase the cooling by a factor of 10 instead of reducing the heating, but this does not change the results concerning fragmentation.

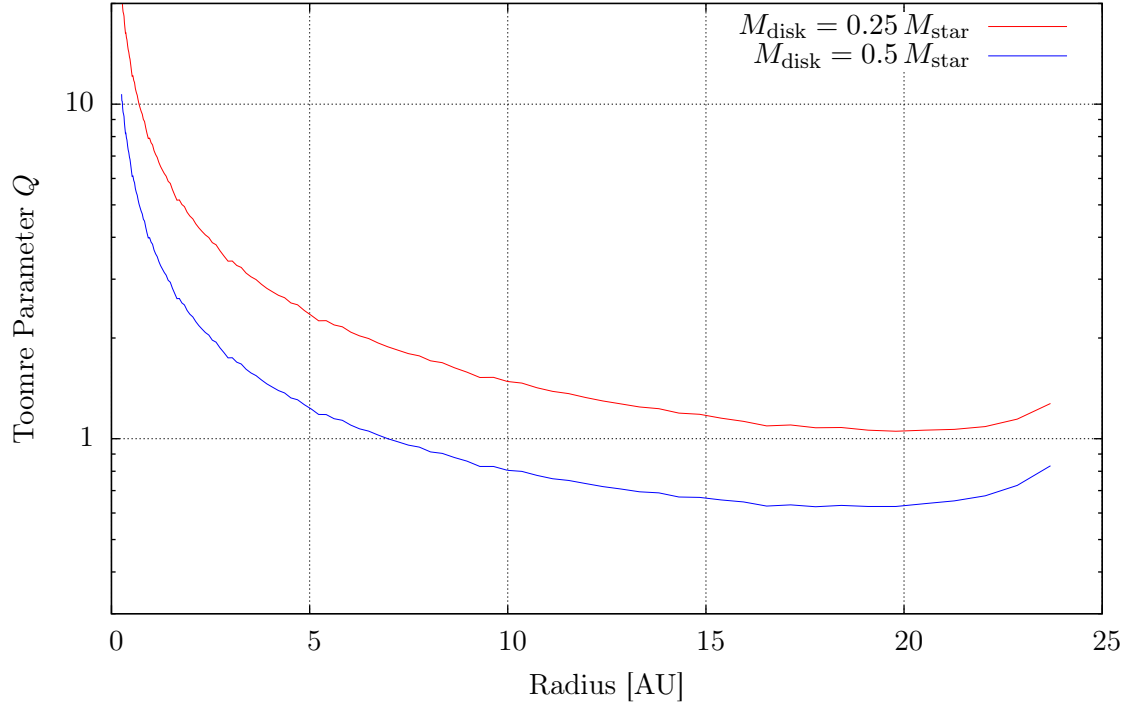


Figure 4.12: Toomre Parameter Q for the $M_{\text{disk}} = 0.25 M_{\text{star}}$ and $0.5 M_{\text{star}}$ disk. The heavier disk satisfies Toomre's criterion for $r \gtrsim 6$ AU whereas the lighter disk does not fit the $Q < 1$ criterion at all.

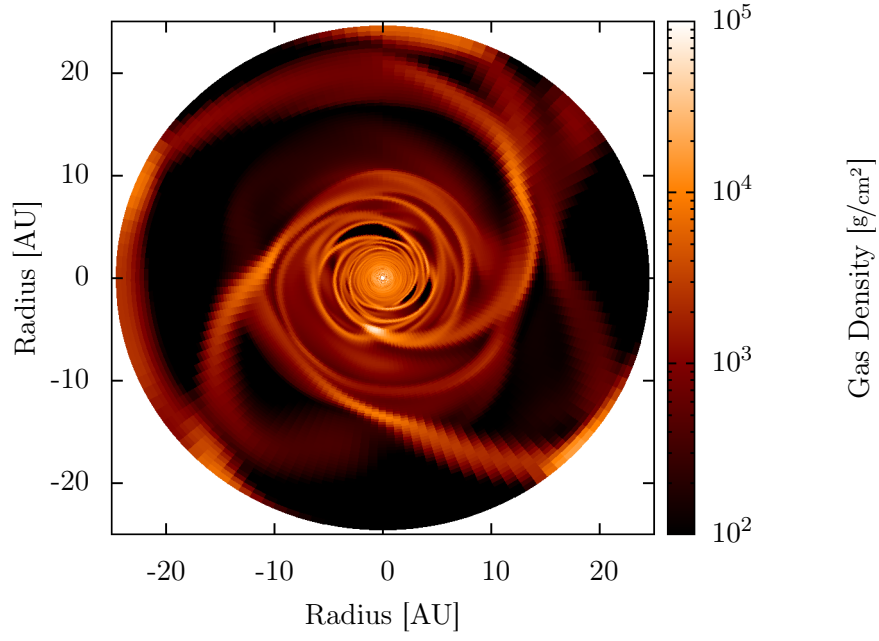


Figure 4.13: First signs of fragmentation of a $0.25 M_{\text{star}}$ disk after 230 orbits at $r = 1$ AU with β -Cooling and no viscous dissipation. Figure 4.14 displays the Toomre parameter at this time-step.

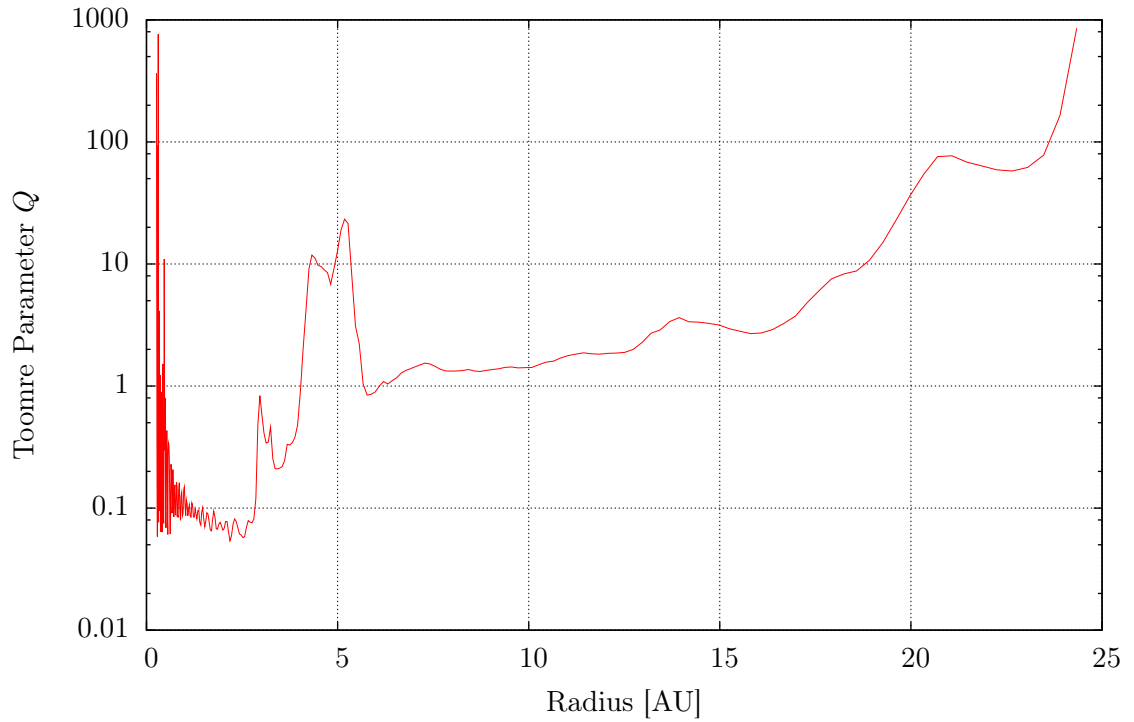


Figure 4.14: Toomre parameter Q of a $0.25 M_{\text{star}}$ disk after 230 orbits at $r = 1$ AU with β -Cooling and no viscous dissipation.

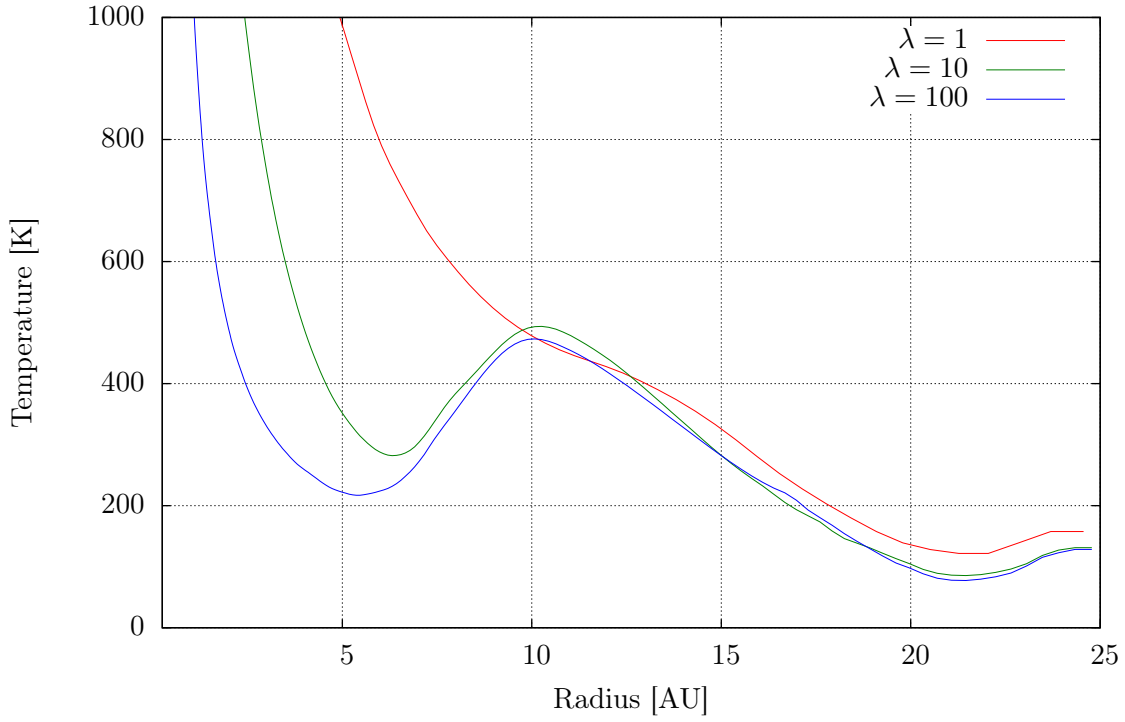


Figure 4.15: Azimuthally averaged temperature of the $0.25 M_{\text{star}}$ disk after 500 orbits at $r = 1$ AU with different damping factors λ of the viscous heating. As expected, disk with less heating have lowered temperatures, but the difference between factor 10 and 100 is vanishing for $r > 15$ AU.

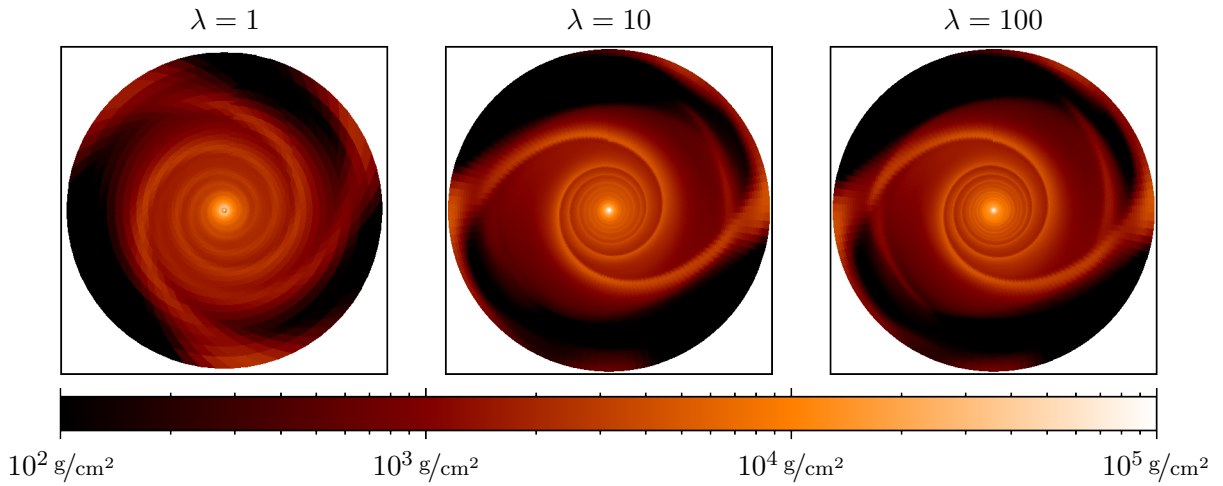


Figure 4.16: Surface density evolution of the $0.25 M_{\text{star}}$ disk after 500 orbits at $r = 1$ AU with different reduction factors λ of the viscous heating. The left panel is with normal viscous heating whereas the middle panel is reduced by a factor of 10 and the right panel by a factor of 100.

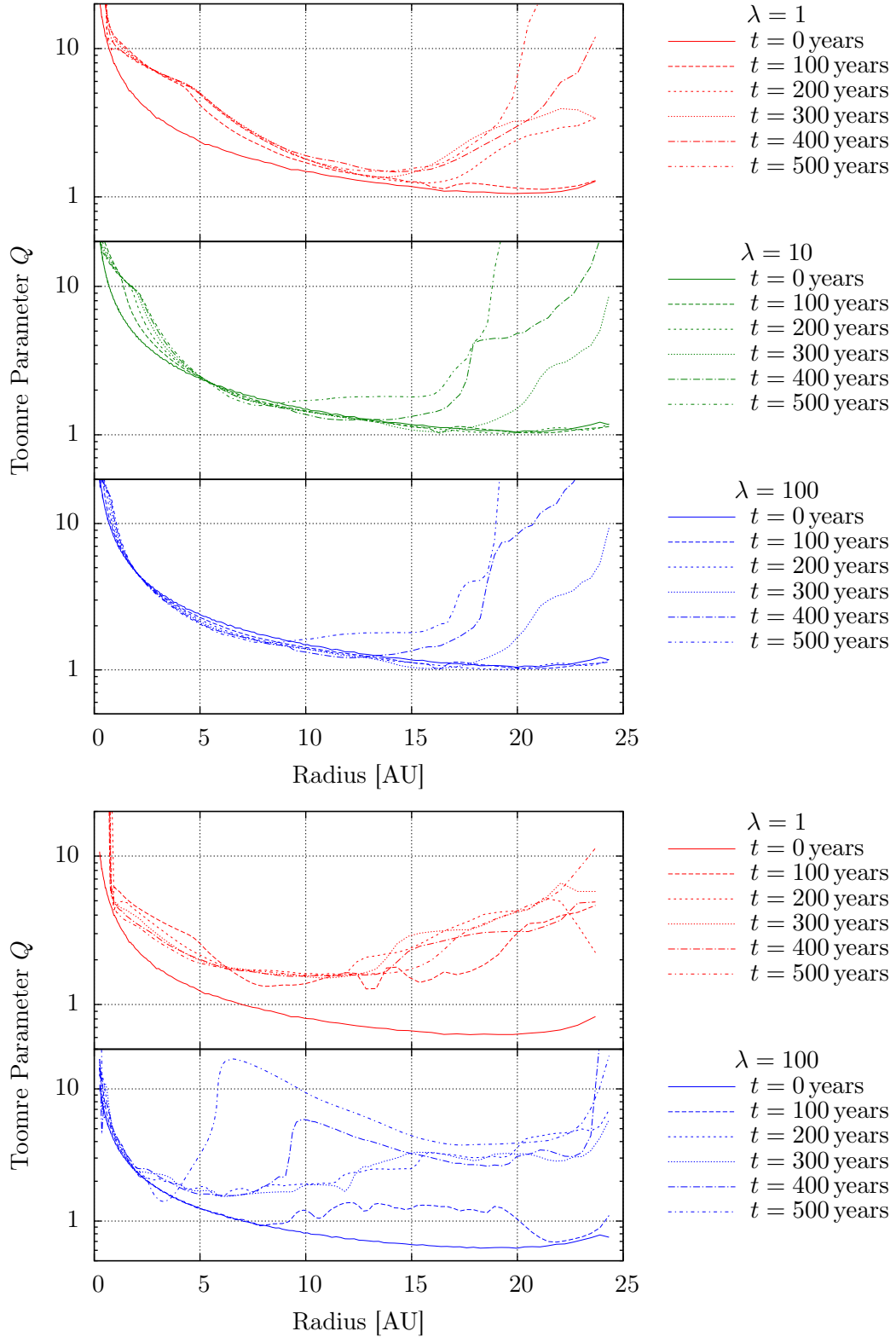


Figure 4.17: Evolution of disk's Toomre parameter over time for the different values of λ . The upper panels display the values for the $0.25 M_{\text{star}}$ disk whereas the lower panels for the $0.5 M_{\text{star}}$ mass disk. For the $0.5 M_{\text{star}}$ disk no $\lambda = 10$ calculation has been done. The increase on the outer boundary is not caused by the FARGO open boundary conditions.

5 Summary

In this work we simulated two-dimensional accretion disks around host stars with the hydrodynamic code **FARGO**, which solves the Navier-Stokes equations. The code has been modified to include self-gravity and an energy equation with viscous heating and local radiative cooling and as an alternative simple β -cooling where cooling timescales have a fixed proportionality to the orbital timescale. For the viscosity of the disk, we used the phenomenological approach of [Shakura and Sunyaev \(1973\)](#), known as the α -model.

In the first step, we simulated isothermal disks with no evolution of energy to test the fragmentation disk under isothermal conditions. If the disks satisfies Toomre's stability criterion they do not fragment whereas if they do not satisfy it, they fragment.

In further simulations we examined the dependency of the α parameter of the viscosity model on the fragmentation of the disk ranging from $1 r_{\text{jup}}$ to $10 r_{\text{jup}}$ with the use of the energy equation with viscous heating and local radiative cooling. Whatever value of α we used in range range of 0.005 to 0.5 we did not get any fragmentation.

Last but not least we performed calculations in analogy to simulations done by [Rice et al. \(2005\)](#) with radial disk extent ranging from 0.25 AU to 25 AU. In comparison to [Rice et al.](#) who used a SPH code and β -cooling we used the **FARGO** grid code and local radiative cooling. Whereas [Rice et al.](#) got fragmentation depending on the value β we did not obtain any fragmentation at all.

We therefore conclude that adding a more realistic cooling method (apart from β -cooling) makes the disk less likely to fragment. As all our non-isothermal simulations had a radial extent not exceeding $10 r_{\text{jup}} = 52 \text{ AU}$, fragmentation could occur for radii larger than that. This has to be checked in future calculations.

Also most of the calculations have been done using the original **FARGO** open boundary condition. To check the influence of the boundary effects most of the calculations should be redone using more realistic open boundary conditions.

Acknowledgements

While working on this diploma thesis I was supervised excellently by Prof. Dr. Wilhelm Kley. I benefited from the good atmosphere within the Computational Physics group at the Institute for Astronomy and Astrophysics Tübingen. For questions concerning the **FARGO** code I received excellent answers and explanations from Aurélien Crida and Clément Baruteau by e-mail and on their visit at the conference “Planet Formation and Evolution: The Solar System and Extrasolar Planets” in Tübingen. Aaron C. Boley and Giuseppe Lodato gave me valuable hints on their visits here in Tübingen.

I received financial support for my trip to the “Winter workshop on planetary astrophysics” in Beijing, China from the DFG Forschergruppe FOR 759 “The Formation of Planets: The Critical First Growth Phase” and the Kavli Institute for Astronomy and Astrophysics at Peking University.

Special thanks go to my whole family, in particular my girlfriend Anneke, my parents Luise and Gerd and my brothers Thomas und Markus, for supporting me during my studies and the work of this diploma thesis. Furthermore I want to thank my fellows for fruitful discussions about my thesis and other problems during our studies. I want to mention here Fabian Amann, Philipp Buchegger, Stefan Christmann, Stephan Hartmann, Niels Oppermann, Daniel Pröpper, Patrick Ruoff and Alexander Seizinger.

References

- Bally, J., L. Testi, A. Sargent, and J. Carlstrom 1998.
Disk Mass Limits and Lifetimes of Externally Irradiated Young Stellar Objects Embedded in the Orion Nebula.
The Astronomical Journal **116**, 854–859.
- Baruteau, C. 2008.
Toward predictive scenarios of planetary migration.
Ph. D. thesis, CEA Saclay.
- Bate, M. R., S. H. Lubow, G. I. Ogilvie, and K. A. Miller 2003.
Three-dimensional calculations of high- and low-mass planets embedded in protoplanetary discs.
Royal Astronomical Society, Monthly Notices **341**, 213–229.
- Binney, J., and S. Tremaine 1987.
Galactic dynamics.
Princeton University Press.
- Bodenheimer, P., and J. B. Pollack 1986.
Calculations of the accretion and evolution of giant planets The effects of solid cores.
Icarus **67**, 391–408.
- Briceño, C., A. K. Vivas, N. Calvet, L. Hartmann, R. Pacheco, D. Herrera, L. Romero, P. Berlind, G. Sánchez, J. A. Snyder, and P. Andrews 2001.
The CIDA-QUEST Large-Scale Survey of Orion OB1: Evidence for Rapid Disk Dissipation in a Dispersed Stellar Population.
Science **291**, 93–97.
- D’Angelo, G., T. Henning, and W. Kley 2003.
Thermohydrodynamics of Circumstellar Disks with High-Mass Planets.
The Astrophysical Journal **599**, 548–576.
- Durisen, R. H., A. P. Boss, L. Mayer, A. F. Nelson, T. Quinn, and W. K. M. Rice 2007.
Gravitational Instabilities in Gaseous Protoplanetary Disks and Implications for Giant Planet Formation.
Protostars and Planets V, 607–622.
- Eisner, J. A., and J. M. Carpenter 2003.
Distribution of Circumstellar Disk Masses in the Young Cluster NGC 2024.
The Astrophysical Journal **598**, 1341–1349.
- Eisner, J. A., and J. M. Carpenter 2006.
Massive Protoplanetary Disks in the Trapezium Region.
The Astrophysical Journal **641**, 1162–1171.
- Eisner, J. A., L. A. Hillenbrand, J. M. Carpenter, and S. Wolf 2005.
Constraining the Evolutionary Stage of Class I Protostars: Multiwavelength Observations and Modeling.
The Astrophysical Journal **635**, 396–421.

- Gammie, C. F. 2001.
Nonlinear Outcome of Gravitational Instability in Cooling, Gaseous Disks.
The Astrophysical Journal **553**, 174–183.
- Haghighipour, N., and A. P. Boss 2003a.
On Gas Drag-Induced Rapid Migration of Solids in a Nonuniform Solar Nebula.
The Astrophysical Journal **598**, 1301–1311.
- Haghighipour, N., and A. P. Boss 2003b.
On Pressure Gradients and Rapid Migration of Solids in a Nonuniform Solar Nebula.
The Astrophysical Journal **583**, 996–1003.
- Haisch, K. E., Jr., E. A. Lada, and C. J. Lada 2001.
Disk Frequencies and Lifetimes in Young Clusters.
The Astrophysical Journal **553**, L153–L156.
- Hawley, J. F., L. L. Smarr, and J. R. Wilson 1984.
A numerical study of nonspherical black hole accretion. I Equations and test problems.
The Astrophysical Journal **277**, 296–311.
- Hubeny, I. 1990.
Vertical structure of accretion disks - A simplified analytical model.
The Astrophysical Journal **351**, 632–641.
- Jeans, J. H. 1902.
The Stability of a Spherical Nebula.
Royal Society of London Philosophical Transactions Series A **199**, 1–53.
- Johnson, B. M., and C. F. Gammie 2003.
Nonlinear Outcome of Gravitational Instability in Disks with Realistic Cooling.
The Astrophysical Journal **597**, 131–141.
- Klahr, H. H., and P. Bodenheimer 2003.
Turbulence in Accretion Disks: Vorticity Generation and Angular Momentum Transport via the Global Baroclinic Instability.
The Astrophysical Journal **582**, 869–892.
- Kley, W. 2008a.
Planetenentstehung.
Lecture script.
- Kley, W. 2008b.
Theoretische Astrophysik.
Lecture script.
- Kley, W., and A. Crida 2008.
Migration of protoplanets in radiative discs.
Astronomy and Astrophysics **487**, L9–L12.
- Kley, W., M. H. Lee, N. Murray, and S. J. Peale 2005.
Modeling the resonant planetary system GJ 876.
Astronomy and Astrophysics **437**, 727–742.

- Lin, D. N. C., and J. Papaloizou 1985.
On the dynamical origin of the solar system.
In D. C. Black & M. S. Matthews (Ed.), *Protostars and Planets II*, pp. 981–1072.
- Lodato, G., and W. K. M. Rice 2004.
Testing the locality of transport in self-gravitating accretion discs.
Royal Astronomical Society, Monthly Notices **351**, 630–642.
- Lynden-Bell, D., and J. E. Pringle 1974.
The evolution of viscous discs and the origin of the nebular variables.
Royal Astronomical Society, Monthly Notices **168**, 603–637.
- Masset, F. 2000.
FARGO: A fast eulerian transport algorithm for differentially rotating disks.
Astronomy and Astrophysics Supplement **141**, 165–173.
- Mayer, L., T. Quinn, J. Wadsley, and J. Stadel 2004.
The Evolution of Gravitationally Unstable Protoplanetary Disks: Fragmentation and Possible Giant Planet Formation.
The Astrophysical Journal **609**, 1045–1064.
- Mayor, M., and D. Queloz 1995.
A Jupiter-mass companion to a solar-type star.
Nature **378**, 355–359.
- Mejía, A. C., R. H. Durisen, M. K. Pickett, and K. Cai 2005.
The Thermal Regulation of Gravitational Instabilities in Protoplanetary Disks. II. Extended Simulations with Varied Cooling Rates.
The Astrophysical Journal **619**, 1098–1113.
- Mihalas, D., and B. Weibel-Mihalas 1999.
Foundations of Radiation Hydrodynamics.
Dover Publications.
- Nelson, R. P., J. C. B. Papaloizou, F. Masset, and W. Kley 2000.
The migration and growth of protoplanets in protostellar discs.
Royal Astronomical Society, Monthly Notices **318**, 18–36.
- Osorio, M., P. D'Alessio, J. Muzerolle, N. Calvet, and L. Hartmann 2003.
A Comprehensive Study of the L1551 IRS 5 Binary System.
The Astrophysical Journal **586**, 1148–1161.
- Papaloizou, J. C., and G. J. Savonije 1991.
Instabilities in self-gravitating gaseous discs.
Royal Astronomical Society, Monthly Notices **248**, 353–369.
- Pollack, J. B., O. Hubickyj, P. Bodenheimer, J. J. Lissauer, M. Podolak, and Y. Greenzweig 1996.
Formation of the Giant Planets by Concurrent Accretion of Solids and Gas.
Icarus **124**, 62–85.

- Pringle, J. E. 1981.
Accretion discs in astrophysics.
Annual review of astronomy and astrophysics **19**, 137–162.
- Rice, W. K. M., P. J. Armitage, M. R. Bate, and I. A. Bonnell 2003.
The effect of cooling on the global stability of self-gravitating protoplanetary discs.
Royal Astronomical Society, Monthly Notices **339**, 1025–1030.
- Rice, W. K. M., G. Lodato, and P. J. Armitage 2005.
Investigating fragmentation conditions in self-gravitating accretion discs.
Royal Astronomical Society, Monthly Notices **364**, L56–L60.
- Rodríguez, L. F., L. Loinard, P. D’Alessio, D. J. Wilner, and P. T. P. Ho 2005.
IRAS 16293-2422B: A Compact, Possibly Isolated Protoplanetary Disk in a Class 0 Object.
The Astrophysical Journal **621**, L133–L136.
- Shakura, N. I., and R. A. Sunyaev 1973.
Black holes in binary systems. Observational appearance.
Astronomy and Astrophysics **24**, 337–355.
- Shu, F. H. 1992.
The Physics of Astrophysics I. Radiation.
Mill Valley: University Science Books.
- Stone, J. M., and M. L. Norman 1992.
ZEUS-2D: A radiation magnetohydrodynamics code for astrophysical flows in two space dimensions. I - The hydrodynamic algorithms and tests.
Astrophysical Journal Supplement Series **80**, 753–790.
- Toomre, A. 1964.
On the gravitational stability of a disk of stars.
The Astrophysical Journal **139**, 1217–1238.
- van Leer, B. 1977.
Towards the ultimate conservative difference scheme. III - Upstream-centered finite-difference schemes for ideal compressible flow. IV - A new approach to numerical convection.
Journal of Computational Physics **23**, 263–299.
- Weidenschilling, S. J. 1977.
Aerodynamics of solid bodies in the solar nebula.
Royal Astronomical Society, Monthly Notices **180**, 57–70.
- Yorke, H. W., and P. Bodenheimer 1999.
The Formation of Protostellar Disks. III. The Influence of Gravitationally Induced Angular Momentum Transport on Disk Structure and Appearance.
The Astrophysical Journal **525**, 330–342.

List of Figures

1.1	Distribution of extrasolar planets (red points) as of February 9 th , 2010. The planets of the solar system (blue points) are displayed for comparison (www.exoplanet.eu)	9
1.2	Hubble Space Telescope images of four protoplanetary disks around young stars in the Orion nebula, located 1.500 light-years away. Credit by Mark McCaughrean (Max-Planck-Institute for Astronomy), C. Robert O'Dell (Rice University), and NASA	10
1.3	Artist's concept of a protoplanetary disk, NASA	11
2.1	Stability diagram for clumping into axisymmetric rings by a self-gravitating differentially rotating, gaseous disk. The lighter read area is the unstable region and the red curve shows marginal stability. The white area is stable. Short-wavelength disturbances are stabilized by the effects of pressure whereas long-wavelength disturbances are stabilized by the effects of rotation.	20
3.1	Schematic of staggered grid used in FARGO. The gray cells represent the ghost cells used in radial direction (see section 3.5) whereas the white cells represent the active cells on which calculations are done. Scalar quantities are stored cell centered (dots) as vector quantities are stored on the cell borders (arrows).	28
3.2	Illustrating the FARGO-Algorithm: The different rings (colored in different gray) rotate at different mean velocities, but all cells in one ring have the same mean velocity but different residual velocities. The disk rotates differentially and therefore the inner rings rotate at higher velocities than the outer rings.	30
3.3	One-dimensional illustration of the alias issue. In the upper left panel is the surface density with a single singular mass density at $r = 0.1$. The upper right panel displays the periodic kernel. The lower panel shows the numerical potential obtained by FFT (blue crosses) and the analytical calculated potential (red curve).	33
3.4	Opacity $\kappa(T)$ at density $\rho = 1 \cdot 10^{-8} \text{ g/cm}^3$. The vertical lines separate the different regimes described in table 3.1. The dotted red curve show the power-laws for each region whereas the blue curve is the smoothed function used in the code.	37
3.5	Comparison of surface density and temperature of the relaxed model with calculations done by Kley and Crida (2008)	39
4.1	Surface density (upper panel) and Toomre parameter (lower panel) for the isothermal model at $t = 0$ with the original FARGO open boundary condition. The fluctuations are caused by the 10 % random initialization. The $0.2 M_{\text{star}}$ disk (purple curve) satisfies the Toomre criterion ($Q < 1$) for $r > 1 \text{ AU}$ whereas the $0.4 M_{\text{star}}$ disk (red curve) satisfies the Toomre for all radii.	42
4.2	Angular rotation rate Ω in terms of Kepler rate Ω_K (see equation 2.2) at $t = 0$. The angular rate is self-gravity compensated and therefore not equal to Ω_K .	43
4.3	Time evolution of the disk's surface density with masses of $0.1 M_{\text{star}}$ (upper row), $0.2 M_{\text{star}}$ (middle row) and $0.4 M_{\text{star}}$ (lower row) with the original FARGO open boundary condition . The disks ranges from 0.5 AU to 2.5 AU. The $0.1 M_{\text{star}}$ mass disk doesn't fragment after the simulation of 50 years, whereas the $0.2 M_{\text{star}}$ disk fragments after about 20 years. The $0.4 M_{\text{star}}$ disk fragments after a very short time of only a few years. The color-axis of the different disks has been adjusted to have the same coloring at the start point.	44

4.4	Time evolution of the disk's surface density with masses of $0.1 M_{\text{star}}$ (upper row), $0.2 M_{\text{star}}$ (middle row) and $0.4 M_{\text{star}}$ (lower row) with open boundary condition . The disks ranges from 0.5 AU to 2.5 AU. The $0.1 M_{\text{star}}$ mass disk doesn't fragment after the simulation of 50 years. The $0.2 M_{\text{star}}$ disk shows unregular spiral arms, but does not fragment into clumps even after 500 years. The $0.4 M_{\text{star}}$ disk fragments after a very short time of only a few years. The color-axis of the different disks has been adjusted to have the same coloring at the start point.	45
4.5	Evolution of disk mass over time. The higher the disk mass the more mass is lost over time. The $0.1 M_{\text{star}}$ disk loses only 18 % of mass in the first 50 years whereas the $0.2 M_{\text{star}}$ loses 37 % and the $0.4 M_{\text{star}}$ even 91 %.	46
4.6	Time evolution of the disk's surface density with a mass of $0.5 M_{\text{star}}$ and a large disk with radial extent ranging from 10 AU to 100 AU. The fragmentation occurs within 1000 years.	47
4.7	Evolution of disk mass over time of the $0.5 M_{\text{star}}$ mass disk. Nearly all mass lost is lost during the first 5000 years.	48
4.8	Surface density and temperature of the model at initialization (red curve) and at thermal equilibrium (blue curves) for different α values. The density fluctuations in the blue curves for radii larger than $\sim 7 r_{\text{jup}}$ are caused by oscillations around the equilibrium value.	50
4.9	Evolution of total disk energy over time until equilibrium. The disks with small α values needed much longer to come to thermal equilibrium. Disks with large α are oscillating around a quasi equilibrium.	51
4.10	Toomre Parameter Q for $0.1 M_{\text{star}}$ and $0.2 M_{\text{star}}$ disk with $\alpha = 0.02$ in thermal equilibrium. Both satisfies Toomre's criterion for $r \gtrsim 4.5$ AU.	51
4.11	Time evolution of the disk's surface density after 500 years different values of α	52
4.12	Toomre Parameter Q for the $M_{\text{disk}} = 0.25 M_{\text{star}}$ and $0.5 M_{\text{star}}$ disk. The heavier disk satisfies Toomre's criterion for $r \gtrsim 6$ AU whereas the lighter disk does not fit the $Q < 1$ criterion at all.	54
4.13	First signs of fragmentation of a $0.25 M_{\text{star}}$ disk after 230 orbits at $r = 1$ AU with β -Cooling and no viscous dissipation. Figure 4.14 displays the Toomre parameter at this time-step.	55
4.14	Toomre parameter Q of a $0.25 M_{\text{star}}$ disk after 230 orbits at $r = 1$ AU with β -Cooling and no viscous dissipation.	55
4.15	Azimuthally averaged temperature of the $0.25 M_{\text{star}}$ disk after 500 orbits at $r = 1$ AU with different damping factors λ of the viscous heating. As expected, disk with less heating have lowered temperatures, but the difference between factor 10 and 100 is vanishing for $r > 15$ AU.	56
4.16	Surface density evolution of the $0.25 M_{\text{star}}$ disk after 500 orbits at $r = 1$ AU with different reduction factors λ of the viscous heating. The left panel is with normal viscous heating whereas the middle panel is reduced by a factor of 10 and the right panel by a factor of 100.	56
4.17	Evolution of disk's Toomre parameter over time for the different values of λ . The upper panels display the values for the $0.25 M_{\text{star}}$ disk whereas the lower panels for the $0.5 M_{\text{star}}$ mass disk. For the $0.5 M_{\text{star}}$ disk no $\lambda = 10$ calculation has been done. The increase on the outer boundary is not caused by the FARGO open boundary conditions.	57